Structural basis for loading and inhibition of a bacterial T6 SS phospholipase effector by the VgrG spike

Nicolas Flaugnatti, Chiara Rapisarda, Martial Rey, Solène G Beauvois, Viet Anh Nguyen, Stéphane Canaan, Eric Durand, Julia Chamot-rooke, E. Cascales, Rémi Fronzes, et al.

Structural basis for loading and inhibition of a bacterial T6SS phospholipase effector by the VgrG spike

Running title: T6SS VgrG-effector complex formation

Nicolas Flaugnatti[1,4,†], Chiara Rapisarda[2,5†], Martial Rey[3], Solène G. Beauvois[1], Viet Anh Nguyen[1], Stéphane Canaan[1], Eric Durand[1], Julia Chamot-Rooke[3], Eric Cascales[1], Rémi Fronzes[2,*], Laure Journet[1,**]

[1] Laboratoire d'Ingénierie des Systèmes Macromoléculaires, Institut de Microbiologie de la Méditerranée, Aix-Marseille Université – CNRS, UMR 7255, 31 Chemin Joseph Aiguier, 13402 Marseille Cedex 20, France

[2] Institut Européen de Chimie et Biologie, University of Bordeaux, Pessac, France, CNRS UMR 5234 Microbiologie Fondamentale et Pathogénicité, Bordeaux, France

[3] Mass Spectrometry for Biology Unit, Institut Pasteur, CNRS USR 2000, CITECH, 28, rue du Dr. Roux 75015, Paris, France

[4] Present address: Laboratory of Molecular Microbiology, Global Health Institute, School of Life Sciences, Ecole Polytechnique Fédérale de Lausanne (EPFL), Lausanne, Switzerland

[5] Present address: UCB Pharma, Slough, SL1 3WE, UK

[†] These authors contributed equally: Nicolas Flaugnatti, Chiara Rapisarda

[*] Corresponding author: Tel: +33 5 40 00 30 08; E-mail: r.fronzes@iecb.u-bordeaux.fr

[**] Corresponding author: Tel: +33 4 91 16 44 62; E-mail: ljournet@imm.cnrs.fr

ABSTRACT

The bacterial Type VI secretion system (T6SS) is a macromolecular machine that injects effectors into prokaryotic and eukaryotic cells. The mode of action of the T6SS is similar to contractile phages: the contraction of a sheath structure pushes a tube topped by a spike into target cells. Effectors are loaded onto the spike or confined into the tube. In enteroaggregative *E. coli*, the Tle1 phospholipase binds the C-terminal extension of the VgrG trimeric spike. Here we purify the VgrG-Tle1 complex and show that a VgrG trimer binds three Tle1 monomers and inhibits their activity. Using covalent cross-linking coupled to high-resolution mass spectrometry we provide information on the sites of contact and further identify the requirement for a Tle1 N-terminal secretion sequence in complex formation. Finally, we report the 2.6-Å resolution cryo-electron microscopy tri-dimensional structure of the $(VgrG)_3$-$(Tle1)_3$ complex revealing how the effector binds its cargo, and how VgrG inhibits Tle1 phospholipase activity. The inhibition of Tle1 phospholipase activity once bound to VgrG suggests that Tle1 dissociation from VgrG is required upon delivery.

Keywords: type VI secretion system/bacterial competition/cryo-electron microscopy/ bacterial toxin/protein secretion

INTRODUCTION

The Type VI secretion system (T6SS) is a multiprotein secretion nano-machine used by many Gram-negative bacteria to deliver toxins in a contact-dependent manner directly into target cells. The T6SS can target both eukaryotic and prokaryotic cells, secreting effectors that degrade the peptidoglycan (amidases, glycoside hydrolase), membranes (phospholipases A_1, A_2 and D), or DNA (DNase) (Russell *et al*, 2014; Durand *et al*, 2014; Cianfanelli *et al*, 2016; Hachani *et al*, 2016). Some anti-host effectors interfere with eukaryotic cytoskeleton dynamics (actin, microtubules), leading to phagocytosis inhibition or promoting invasion. (Russell *et al*, 2014; Durand *et al*, 2014; Cianfanelli *et al*, 2016; Hachani *et al*, 2016). The T6SS secretion of anti-bacterial effectors allows bacteria to eliminate competitors, to acquire nutrients, new DNA or metal, thus favoring the colonization of specific niches (Russell *et al*, 2014; Durand *et al*, 2014; Cianfanelli *et al*, 2016; Hachani *et al*, 2016).

T6SS biogenesis needs at least 14 different proteins. These subunits assemble two sub-complexes: a membrane complex anchored in the envelope (Durand *et al*, 2015; Rapisarda *et al*, 2019), on which is docked a platform that controls the assembly of a contractile tail tube/sheath structure (Brunet *et al*, 2015; Logger *et al*, 2016; Taylor *et al*, 2016; Nguyen *et al*, 2017; Nazarov *et al*, 2018; Basler *et al*, 2012). The tail tube/sheath complex comprises an inner tube made of Hcp hexamers covered by a sheath and topped by a needle spike constituted of a VgrG trimer and a PAAR-domain protein (Zoued *et al*, 2014; Ho *et al*, 2014). The tail sheath assembles in an extended conformation and its contraction propels the inner tube, the spike and toxins towards target cells. Self-protection is assured by immunity proteins that specifically bind and inhibit their corresponding effectors. A few T6SS effectors are fused to the Hcp, VgrG, or PAAR proteins and are therefore delivered into the recipient cell as domains of syringe components (Pukatzki *et al*, 2006; Blondel *et al*, 2009; Suarez *et al*, 2010; Brooks *et al*, 2013; Dong *et al*, 2013; Shneider *et al*, 2013; Ma *et al*, 2017). However,

most T6SS effectors are independent polypeptides. Upon T6SS assembly these effectors are loaded within the lumen of the Hcp tube or bind the VgrG/PAAR spike and are then transported as cargo (Durand *et al*, 2014; Cianfanelli *et al*, 2016; Ho *et al*, 2014). Small effectors (< 20 kDa), such as the *Pseudomonas aeruginosa* Tse2 toxin, have been shown to fill the internal hole of Hcp hexamers (Silverman *et al*, 2013) whereas others have been demonstrated to indirectly interact with VgrG. Binding of these effectors is mediated by specific adaptors (Alcoforado Diniz & Coulthurst, 2015; Liang *et al*, 2015; Unterweger *et al*, 2015; Bondage *et al*, 2016). These adaptors are not secreted components but are rather required for the secretion of their cognate effectors, suggesting a role in loading effectors to VgrG prior to translocation. A complex constituted of the PAAR-fused Tse6 effector, the EagT6 adaptor, the immunity to Tse6 and EF-Tu was recently visualized by negative stain electron microscopy (EM). It forms a horseshoe-like structure at the tip of the VgrG trimer (Whitney *et al*, 2015). The cryo-EM structure of Tse6-EagT6 in complex with VgrG was further determined (Quentin *et al*, 2018).

We recently identified Tle1, a periplasmic-acting phospholipase A_1 (PLA1) antibacterial effector of the enteroaggregative *E. coli* (EAEC) T6SS-1 (Flaugnatti *et al*, 2016). We showed that Tle1 is transported into the periplasm of target cells using the VgrG spike protein as carrier. By contrast to other VgrG-dependent effectors, Tle1 interacts directly with VgrG, without the need for a PAAR or adaptor protein. VgrG from EAEC possesses a C-terminal extension that comprises a DUF2345 and a transthyretin-like domain (TTR) responsible for the interaction with Tle1 (Flaugnatti *et al*, 2016). Here, we report the purification of the VgrG-Tle1 complex and show that three Tle1 effectors bind to the VgrG trimer. Our data reveal that VgrG inhibits Tle1 PLA1 activity and hence that Tle1 needs to be dissociated from its carrier once in the target cell. Using a combined approach of cross-linking mass spectrometry, deletion studies and functional assays, we identify the motifs involved in VgrG-

Tle1 interaction, confirming the importance of the VgrG TTR domain and highlighting an N-terminal interaction motif within Tle1. Finally, we present the cryo-EM structure of Tle1 bound to the VgrG needle.

RESULTS

Purification of the VgrG-Tle1 complex reveals that three Tle1 bind to the VgrG trimer

We previously showed that Tle1 from EAEC interacts directly with the C-terminal domain extension of the VgrG spike protein (Flaugnatti *et al*, 2016). To gain further insight into the VgrG-Tle1 complex, affinity-tagged VgrG and Tle1 proteins were co-produced in *E. coli*. The position of the affinity tag on each protein was rationally chosen to maintain the VgrG-Tle1 interaction: a Strep-tagII was fused to the N-terminus of VgrG (^{S}VgrG) to maintain the C-terminal Tle1-interacting motif available, and a 6×His tag was fused to the Tle1 C-terminus (Tle1^{H}), as previous bacterial two-hybrid (BACTH) analysis suggested that T25/T18 fusion at the N-terminus of Tle1 protein impaired the interaction with VgrG (Flaugnatti *et al*, 2016). A complex containing both ^{S}VgrG and Tle1^{H} was purified to homogeneity using a two-step affinity purification and gel filtration (Fig EV1A). When subjected to size exclusion chromatography analyses, ^{S}VgrG separated with an apparent mass of ~ 500 kDa (Fig EV1B, black line; Appendix Fig S1), which is higher than the 280-kDa theoretical mass of a VgrG trimer. This could be due to an artefact of the gel filtration technique, the elongated-shape structure of the VgrG β-helix (Leiman *et al*, 2009; Uchida *et al*, 2014; Spínola-Amilibia *et al*, 2016), or this species may correspond to a dimer of a VgrG trimer. Once bound to Tle1^{H}, we observed an increase in the apparent molecular mass (Fig EV1B, blue line). Native-purified Tle1 was previously shown to be monomeric in solution, with an apparent molecular mass of 66 kDa (Flaugnatti *et al*, 2016). Taken together, these results suggest that several Tle1 proteins are bound to the VgrG trimer. To provide further

information on the stoichiometry of the ^{S}VgrG-Tle1^{H} complex, we performed quantitative in-gel SYPRO Ruby staining. This analysis of the purified ^{S}VgrG-Tle1^{H} complex gave a 1:0.92 molar ratio (Fig EV1C). The approximate 1:1 stoichiometry suggests that three Tle1 effectors are bound to a VgrG trimer.

High-resolution cross-linking mass spectrometry (XL-MS) mapping identifies VgrG-Tle1 sites of contact

To provide detailed information on the VgrG/Tle1 interaction, the ^{S}VgrG-Tle1^{H} complex was subjected to cross-linking with the NNP9 cross-linker (Nury *et al*, 2015). NNP9 was specifically engineered to carry 2 NHS carbamate reactive groups, which are less prone to hydrolysis than widely used NHS-esters, thus improving cross-linking efficiency and performance compared to commercial ones (Nury *et al*, 2015). Mass spectrometry analysis of cross-linked peptides revealed that VgrG and Tle1 establish numerous contacts (Fig 1A, Dataset EV1). In agreement with previous findings demonstrating that Tle1 binds the VgrG C-terminal TTR extension as well as a second upstream motif (Flaugnatti *et al*, 2016), XL-MS showed that Tle1 binds the VgrG TTR motif and a second motif located in the C-terminal part of the gp27-like domain (Fig 1A). Accordingly, Tle1^{H} no longer co-purified with a ^{S}VgrG variant lacking the C-terminal 616-841 residues (^{S}VgrG$_{\Delta CTD}$) (Appendix Fig S2A and B). More importantly, several cross-links involving Lys residues in the VgrG TTR domain and at the Tle1 N-terminus (K29, K30) were detected (Fig 1A and Appendix Fig S3A), suggesting that the VgrG TTR binds the Tle1 N-terminus. Interestingly, a sequence alignment of Tle1 orthologs reveals a striking difference at their N-termini. Compared to specialized Tle1 orthologs that are fused to Hcp, PAAR and VgrG proteins, isolated Tle1 proteins bear an N-terminal 26-amino-acid extension (NT) (Fig 1B and Appendix Fig S3B). As deletion of the Tle1 NT region (Tle1$_{\Delta 1\text{-}26}$) did not impact PLA1 specific activity (Appendix Fig S4), this

region is not necessary for Tle1 folding and activity. Tle1 NT extension is followed by a Lys-rich linker that precedes the Tle1-domain region (Appendix Fig S3). Substitution of these Lysines by Glutamate residues (K28K29K30-to-E28E29E30) did not impair Tle1 antibacterial activity against *E. coli* K12 (Fig 1C), suggesting that the K29 and K30 residues identified by XL-MS are not directly involved in the interaction with VgrG. Rather, the XL-MS data highlight the proximity of the NT and the TTR region in the complex and we hypothesized that the NT region might be an important determinant of a Tle1 secretion signal allowing VgrG recognition and binding. Evidence for the crucial role of this extension was provided by co-immunoprecipitation (Fig 1D) and co-purification (Appendix Fig S2C) assays, which demonstrated that deletion of the Tle1 N-terminal 26 amino-acids strongly affects the interaction with VgrG. To further test the importance of this VgrG interaction motif for the delivery of Tle1, we tested the ability of $Tle1_{\Delta 1\text{-}26}$ to complement a *tle1* knockout mutant in antibacterial competition (Fig 1C). While the production levels of Tle1 and $Tle1_{\Delta 1\text{-}26}$ were comparable, only Tle1 restored the killing defect of the *tle1* knockout mutant. Taken together these results showed that Tle1 binds two regions of VgrG including the C-terminal TTR extension, whereas the Tle1 N-terminal 26-amino-acid region is required for VgrG binding and translocation into target cells.

Cryo-EM structure of the VgrG-Tle1 complex. *Architecture of the VgrG spike-Tle1 complex*. To gain further information on the structure of the VgrG-Tle1 complex, the purified ^{S}VgrG-Tle1^{H} complex was analysed using single particle cryo-EM. The structure of the complex at 2.7-Å resolution overall was obtained by applying no symmetry (Fig EV2A and B). The 2D classes resembled violin bodies and were found in different orientations (Fig EV2A). From the unmasked cryo-EM density we can observe the presence of a D3 symmetry with the dihedral rotational centre found between the two prism-like densities and further

163 strengthened by opposite flexible densities interacting with each other (Fig EV2B and C).
164 This large symmetric complex is 225-Å tall and 150-Å large, and consists of 6 VgrG and 6
165 Tle1 densities as inferred from the gel filtration (Fig EV1B, Fig EV2B and C). This
166 oligomeric state is likely not physiological. The absence of the PAAR capping protein may
167 lead to this tip-to-tip VgrG needle spike interaction. We performed an unmasked refinement
168 to 2.7 Å (Fig EV2B-D) followed by a local refinement on what we will hereby refer to as the
169 physiological complex, consisting of 3 Tle1 and 3 VgrG molecules, and obtained a resolution
170 of 2.6 Å (Fig 2A-C, Fig EV2E). We further locally refined the prism-like density
171 corresponding to VgrG (to 2.3-Å resolution), and one external density belonging to Tle1 (to
172 2.5-Å resolution) (Fig EV2F and G). Thanks to the high resolution of the cryo-EM densities
173 obtained (Fig EV2E-G), we could build *de novo* an atomic model of VgrG amino-acids (aa)
174 491-834 and of the full Tle1 (Fig 2D-H and Fig 3A and B), whose structures were previously
175 unknown.
176 No interpretable cryo-EM density was found for VgrG amino-acids 1-490. This region which
177 is homologous to the gp27-like base followed by the gp5-OB fold-like in the T4 phage,
178 appears to be disordered. Such flexibility may be stabilised by binding of PAAR, and/or by
179 the binding to baseplate components. This region is well conserved amongst the VgrG
180 proteins from different bacterial species and phage families (Leiman *et al*, 2009). We
181 therefore built a model using Phyre2 (Kelley *et al*, 2015), based on the sequence homology
182 (42.5% identity) to the VgrG N-terminus from uropathogenic *E. coli* CFT073, whose
183 structure has been solved by X-ray crystallography (Leiman *et al*, 2009) (Fig 2G).
184 *Structure of the gp5 needle-like domain of VgrG from EAEC*. The atomic model of VgrG (aa
185 491-834) includes the gp5-C-like, DUF2345 and TTR domains predicted by bioinformatic
186 analyses (Flaugnatti *et al*, 2016) (Fig 1A and Fig 2G-H). The region from aa 491 to 760
187 assembles a gp5 needle-like structure corresponding to a three-stranded β-prism with a width

of 30 Å at the tip and 45 Å at the bottom (Fig 2G-H). The β-prism contains 2 antiparallel β-sheets consisting of 5 and 3 strands respectively at aa 491-549 and 726-747 (Fig EV3A). Unique to the EAEC VgrG ($VgrG^{EAEC}$) is also the presence of two long helices that break the β-prism at aa 576-622. The rest of the β-prism is composed of parallel β-sheets that intertwine around each other via sharp β-turns (Fig EV3A). There is no cavity at the centre of the β-prism and the structure is maintained by hydrophobic interactions (Fig 2H). The interaction between the monomers of VgrG, as calculated using PISA (Krissinel & Henrick, 2007), is very strong with a mean surface of interaction of 7150 $Å^2$.

Comparison with the *Pseudomonas aeruginosa* VgrG ($VgrG^{PA}$) structure and with the phage gp5 needle domain reveals several differences. In $VgrG^{PA}$ (Fig EV3B, PDB: 4MTK), the gp-5 needle domain is shorter by 40 Å because it only has a three-strand antiparallel β-sheet at the base of the spike, instead of a 5-strand (in blue, Fig EV3B). In the phage T4 gp5 protein (PDB: 1K28) (Kanamaru *et al*, 2002) there is only one anti-parallel 6-strand β-sheet at the base of the spike and none at the tip (in orange, Fig EV3C). $VgrG^{EAEC}$ is unique also because it has an additional β-sheet TTR domain that binds the effector, (Fig 2G, Fig EV3D). This domain is missing in $VgrG^{PA}$, but it has been shown that the toxin does not directly bind to $VgrG^{PA}$ but is covalently linked to the PAAR component (Whitney *et al*, 2015) (Fig EV3E). In the T4 phage, gp5 has an additional lysozyme domain (Fig EV3F).

Structure of Tle1 bound to VgrG. The Tle1 structure bound to VgrG adopts a thin elongated shape, which is 125-Å tall and 50-Å wide on one side and 75 Å on the other (Fig 3A and B). It can be divided into three distinct domains: the finger N-terminal domain (aa 3-33), the phospholipase catalytic module (aa 33-326 and 411-539), and the lid domain (aa 327-410) (Fig 3A, Fig EV4A). Two loops are missing from the density and are most likely disordered: aa 86-94 and aa 133-143. As shown by cross-link MS, deletion analyses and co-purification (Fig 1D and Appendix Fig S2C), the finger domain is responsible for the interaction with the

213 VgrG TTR domain, and consists of a long loop that is highly flexible (Fig 3A-E, Fig EV4B
214 and C). There is a smaller β-sheet composed of strand 17 at the C-terminus and strand 7 and
215 an incomplete Greek key motif between strands 13-16 and 14-15 (Fig 3, Fig EV4A). The
216 catalytic module has the most compact conformation and contains a classical α/β mixed
217 hydrolase fold, composed of one central β-sheet of 6 β-strands (3-2-4-5-6-8) surrounded by
218 α-helices (Fig 3A and B, Fig EV4A). The lid domain mainly comprises one long twisted
219 antiparallel β-sheet, constituted of three strands (11, 12 and 9 and 10). In between strands 11
220 and 12, α-helix 12 (aa 338-395) mediates the interaction with the VgrG base (Fig 3A and B,
221 Fig EV4A).
222 *A new mechanism for T6SS effector loading on the VgrG spike*. In contrast to the VgrG-
223 chaperone-effector in *P. aeruginosa*, where the effector is fused to PAAR and located at the
224 tip of the needle complex (Fig EV3E), the loading of Tle1 proteins on the VgrG spike is
225 independent of PAAR. Moreover, three molecules of Tle1 are loaded on the VgrG trimer, on
226 the sides of the β-prism (Fig 3F-H and Supplementary Fig EV3D). Tle1 binds VgrG in three
227 different regions (bottom, centre and top) and every VgrG chain interacts with each Tle1
228 monomer (Fig 3F-H, and Table 1). The Tle1 catalytic domain interacts with the two α-helices
229 (581-619) of one VgrG (chain A) and at the level of the β-prism with the two other VgrG
230 monomers (chains B and C) (Fig 3F-H). The lid domain of Tle1 (aa 335-405) interacts only
231 with chains B and C at the level of the anti-parallel β-sheet (Fig 3F-H). Finally, the finger
232 domain of Tle1 (aa 3-33) and the loop of the catalytic domain (aa 225-230) between helix 8
233 and strand 5 interact with the TTR domain of VgrG (aa 778-841) (Fig 3C-E). The TTR
234 domain is globular: it contains 2 sheets composed of 3 and 2 anti-parallel β-strands
235 respectively (Fig 3C-E). The finger domain of Tle1 complements the strands of the TTR
236 domain to form a β-barrel (Fig 3C-E). The surface of interaction of VgrG with Tle1 is 1160
237 $Å^2$ and has a ΔG of -12.2 kcal/M. The TTR-Tle1 interaction is mediated by several hydrogen

238 bonds and salt bridges (Table 1). While VgrG is very stable, the finger domain and the TTR
239 region are very flexible as shown by the b-factor values (Fig EV4B and C), and the local
240 resolution (Appendix Fig S5) as it is connected to the VgrG spike by a very flexible loop
241 whose density was not resolved in the cryo-EM map.
242
243 **Tle1 binding to VgrG inhibits its phospholipase activity**
244 The Tle1 effector exhibits PLA1 activity *in vitro* (Flaugnatti *et al*, 2016). In the cryo-EM
245 structure of VgrG-Tle1, the catalytic module of Tle1 is well defined. It contains the
246 phospholipase catalytic triad in an active conformation as the Ser197 and Asp245 residues are
247 at a <3-Å distance from His310 (Fig 3B). The catalytic triad is located within a cavity that is
248 positively charged at its end, with a hydrophobic entrance (Fig EV5A-B). However,
249 comparison of the cryo-EM structure of $Tle1^{EAEC}$ bound to VgrG to the *P*. *aeruginosa* Tle1
250 ($Tle1^{PA}$) crystal structure suggests that $Tle1^{EAEC}$ PLA1 activity is inhibited by VgrG. In the
251 $Tle1^{PA}$ structure, a specific pocket allows binding of the phosphatidylglycerol moiety of the
252 substrate at close proximity to the active site (Fig 4A) (Hu *et al*, 2014). By contrast, in the
253 $Tle1^{EAEC}$ structure, this pocket is partially occluded by the lid domain. Remarkably, the
254 position of the lid domain is constrained by the binding of its tip (helix 389-393) to VgrG (Fig
255 4B). In agreement with this observation, PLA1 activity of the purified ^{S}VgrG-$Tle1^{H}$ complex
256 was undetectable compared to the purified isolated $Tle1^{H}$ protein (Fig 5A), suggesting that
257 Tle1 binding to VgrG inhibits its activity. To confirm this VgrG-mediated inhibition, isolated
258 $Tle1^{H}$ purified protein was incubated with increasing amounts of purified ^{S}VgrG. Fig 5B
259 shows that $Tle1^{H}$ was inhibited by ^{S}VgrG in a dose-dependent manner, but not with the
260 unrelated lysozyme protein. As a control, we purified $^{S}VgrG_{1\text{-}490,}$ a C-terminal truncated
261 variant of VgrG deleted of the gp5 needle-like domain which mediates most of the contacts

with Tle1^{H} (Fig 5C). In contrast with ^{S}VgrG, incubation of Tle1^{H} with ^{S}VgrG$_{1\text{-}490}$ did not cause Tle1^{H} inhibition (Fig 5B).

Taken together, these results show that the Tle1 phospholipase activity is inhibited by VgrG in the ^{S}VgrG-Tle1^{H} complex, and hence that the Tle1 effectors have to be dissociated from VgrG to exhibit toxic PLA1 activity in the target cell.

DISCUSSION

In this study, we provide a comprehensive picture of a complex between the T6SS VgrG spike protein and the phospholipase effector it recruits for translocation into target cells. We show that these two proteins form a complex with a 1:1 stoichiometry comprising three Tle1 effectors bound to one VgrG trimer, suggesting that three Tle1 effectors are translocated into the target cell at each T6SS firing event. We further show that Tle1 recruitment to VgrG causes the inhibition of its activity. Bioinformatics, high-resolution mass spectrometry mapping and deletion studies combined with protein-protein interaction and functional assays demonstrated the importance of the N-terminal portion of Tle1 as a critical determinant for the interaction with the VgrG C-terminal TTR extension. Finally, we report the high-resolution cryo-EM structure of the Tle1 effector in complex with the needle/TTR portion of the VgrG spike. This structure confirms the importance of the TTR domain of VgrG for its interaction with the N-terminal finger domain of Tle1, and further highlights two previously unidentified regions of contact at the base and at the centre of the needle. Moreover, we provide a structural explanation for Tle1 inhibition by VgrG.

Structural model of the EAEC T6SS baseplate in a pre-firing state

VgrG is not only the spike of the needle but also the hub of the T6SS baseplate (BP) (Taylor *et al*, 2016; Brunet *et al*, 2015). The baseplate is the assembly platform for the tail

tube/sheath complex and is docked to the TssJLM membrane complex (Brunet *et al*, 2015; Zoued *et al*, 2016). The structure of the TssKFGE wedge complex of the baseplate was recently determined by cryo-EM (Cherrak *et al*, 2018). The structure of the fully assembled baseplate, including the VgrG hub surrounded by six wedges, was presented, based on the high-resolution wedge structure (Cherrak *et al*, 2018) and the baseplate lower resolution structure (Nazarov *et al*, 2018). We propose here a structural model of the EAEC T6SS baseplate including VgrG-Tle1 (Appendix Fig S6). Interestingly, the baseplate can readily accommodate the three Tle1 effectors (Appendix Fig S6). We propose that the VgrG-Tle1 structure represents the "pre-firing complex".

A new mode of T6SS substrate loading.

The VgrG-Tle1 complex represents the first example of direct binding of an effector on VgrG, which in general requires the PAAR subunit or an adaptor protein (Shneider *et al*, 2013; Alcoforado Diniz & Coulthurst, 2015; Liang *et al*, 2015; Unterweger *et al*, 2015; Bondage *et al*, 2016). Tle1 binds to three different regions of VgrG (bottom, centre and top), and the three Tle1 molecules are located on the side of the needle rather than on its tip. This contrasts to the position of PAAR-fused Tse6 effector/adaptor in the *P*. *aeruginosa* VgrG tip complex EM structure (Whitney *et al*, 2015; Quentin *et al*, 2018) (Fig EV3B and E). Tle1 positioning on the VgrG sides and the multiple attachment zones tightly tether Tle1 to the spike, which will be released by some unknown mechanism in the periplasm of the target cell. The non-covalent nature of the bonds may also allow Tle1 to be separated from the VgrG spike to elicit its function. The oxidative nature of the periplasm or the presence of specific chaperones might provide the source for Tle1 dissociation. Further work will need to be carried out to understand the implication of such flexible interactions in VgrG-Tle1 dissociation.

312 The EAEC T6SS-1 cluster also encodes a PAAR protein downstream the Tli1 immunity
313 encoding gene. However, in the VgrG-Tle1 complex characterized here, no PAAR is needed
314 for the three Tle1 proteins to bind to the VgrG trimeric spike. The tip of the needle is free to
315 accommodate a PAAR protein necessary for target cell penetration. In the future, it would be
316 of particular interest to co-purify and image PAAR associated to the VgrG-Tle1 complex.
317
318 In contrast to canonical VgrGs, such as $VgrG^{PA}$, $VgrG^{EAEC}$ bears a C-terminal extension
319 (CTD) comprising DUF2345 and TTR domains, linked to the gp27/gp5 base by two long
320 helices (Fig 2G). As shown in this study, the DUF2345 domain folds as a β-prism and hence
321 extends the length of the $VgrG^{EAEC}$ gp5-like β-helix. This extension, as well as the TTR
322 domain, corresponds to the major binding regions of Tle1. $VgrG^{EAEC}$ is therefore a fusion
323 between a prototypical VgrG and DUF2345/TTR extensions that serve as internal adaptor
324 domains (Bondage *et al*, 2016; Flaugnatti *et al*, 2016; Wettstadt *et al*, 2019). However, there
325 is an additional contact between Tle1 and the base of gp5-C domain of VgrG. The direct
326 binding of Tle1 on $VgrG^{EAEC}$ therefore represents the first report of a new mode of effector
327 loading on the T6SS spike. Similar modes of binding might be predicted. This organization of
328 VgrG C-terminal extension (*i.e*., the presence of two long helices followed by the DUF2345
329 and the TTR domains) corresponds to the COG4532 found at the C-terminal domain of a sub-
330 group of VgrG proteins in Proteobacteria (Boyer *et al*, 2009). This group includes proteins
331 such as the VgrG encoded upstream of a putative Tle3 effector in uropathogenic *E. coli*
332 CFT073, or VgrG2a from *P. aeruginosa* encoded upstream the Tle4-like *tlpE* effector (Wood
333 *et al*, 2019) (Appendix Fig S7). The structural organization of these VgrG proteins and their
334 genetic link to phospholipase-encoding genes suggest that these phospholipases might also be
335 directly recruited to the spike extension for delivery.
336

Tle1 inhibition by VgrG

It is noteworthy that the 3' of the *vgrG* gene overlaps with the *tle1* 5' in EAEC (Flaugnatti *et al*, 2016), suggesting translational coupling of the VgrG and Tle1 proteins, a mechanism evolved to promote protein stabilization or to prevent protein toxicity. Indeed, our results show that the VgrG-bound Tle1 phospholipase is inactive as the catalytic site of Tle1 is masked by the mode of binding to VgrG. Production of the Tle1 phospholipase may have deleterious effect on the cytoplasmic membrane phospholipids, and VgrG-mediated inhibition could be regarded as a surveillance mechanism to prevent phospholipid degradation in the attacker cell. However, previous results have shown that Tle1 cytoplasmic overproduction has no impact on the growth of *E. coli* K-12 cells (Flaugnatti *et al*, 2016). Another hypothesis is that there is no need to inhibit Tle1 but rather a need to protect the catalytic site and to prevent exposition of the hydrophobic entrance. Nevertheless, Tle1 needs to dissociate from VgrG once in the periplasm of the target cell.

In conclusion we have identified a novel mechanism of loading and inhibition in the T6SS Tle1 toxin that establishes a new relationship between the spike and its carrier effector.

MATERIALS AND METHODS

Bacterial strains, growth conditions and chemicals.

Strains used in this study are listed in Appendix Table S1. *E. coli* DH5α, BL21(DE3), and W3110 were used for cloning procedures, protein production, and co-immunoprecipitation, respectively. EAEC strain 17-2 and its isogenic derivatives were used for *in vivo* studies. Cells were grown at 37°C with aeration in LB or in *T6SS-1*-inducing medium (SIM; M9 minimal medium, 0.2% glycerol, 1 µg/mL vitamin B1, 100 µg/mL casaminoacids, 10% LB, supplemented or not with 1.5% bactoagar, ampicillin (100 µg/mL), kanamycin (50 µg/mL), or

chloramphenicol (30 µg/mL). Gene expression from pBAD (Guzman *et al*, 1995) and pOK12 (Vieira & Messing, 1991) derivatives was induced by the addition of 0.02-0.2% of L-arabinose (Sigma-Aldrich) and 100 µM isopropyl-thio-β-D-galactopyrannoside (IPTG, Eurobio), respectively. Gene expression from pETDuet-1 and pRSFDuet-1 (Novagen) derivative vectors was induced by the addition of 1 mM IPTG.

Cloning procedures.

Plasmids and primers used in this study are listed in Appendix Table S1. PCRs were performed using a Biometra thermocycler using the Q5 high-fidelity DNA polymerase (New England Biolabs) and EAEC 17-2 chromosomal DNA as a template. Custom oligonucleotides (Sigma-Aldrich) are listed in Appendix Table S1. pRSF-Tle1^{H} and pET-^{S}VgrG were constructed by a restriction–ligation procedure. The sequence encoding Tle1 was amplified by PCR using 5-NdeI-Tle1 and 3-FseI-Tle1^{H} primers introducing NdeI and FseI sites, respectively and cloned into the pRSFDuet-1 (Novagen) multiple cloning site 2 (MCS2) to yield pRSF-Tle1^{H}. The 3-FseI-Tle1^{H} primer introduces a sequence encoding a 6×His-tag to allow in-frame fusion of Tle1 with a C-terminal hexa-histidine extension. The sequence encoding VgrG was amplified by PCR using primers 5-BamHI-^{S}VgrG and 3-HindIII-VgrG introducing BamHI and HindIII sites, respectively and cloned into the pETDuet-1 MCS1 to yield pET-^{S}VgrG. The 5-BamHI-^{S}VgrG primer introduces a sequence encoding a Strep-tagII to allow in frame fusion of VgrG with a N-terminal Strep-tagII. The same cloning strategy was used for pET-^{S}VgrG$_{\Delta CTD}$ and pET-^{S}VgrG$_{1\text{-}490}$, with the use of primers 5-BamHI-^{S}VgrG and 3-HindIII-VgrG$_{\Delta CTD}$ for pET-^{S}VgrG$_{\Delta CTD}$, and primers 5-BamHI-^{S}VgrG and 3-HindIII-VgrG$_{1\text{-}490}$ for pET-^{S}VgrG$_{1\text{-}490}$. For pBAD18-Tle1Δ1-26$_{VSVG,}$ pBAD18-Tle1Δ1-34$_{VSVG}$ and pRSF-Tle1$_{\Delta 1\text{-}26}{}^{H}$ constructions, the sequence encoding amino-acids 1 to 26 (or 1 to 34) of Tle1 has been deleted from pBAD18-Tle1$_{VSVG}$ (Flaugnatti *et al*, 2016) or pRSF-Tle1^{H} by Quick-

change PCR-based targeted mutagenesis using complementary pairs of oligonucleotides and the Pfu Turbo high-fidelity polymerase (Agilent Technologies). Similarly, the K28-to-E/K29-to-E/K30-to-E substitutions were introduced in the pBAD18-Tle1$_{VSVG}$ plasmid by QuickChange PCR-based targeted mutagenesis. All constructs were verified by restriction analysis and DNA sequencing (Eurofins, MWG).

Antibacterial competition assay.

Antibacterial competition assays were performed as described previously (Flaugnatti *et al*, 2016), using wild-type *E. coli* W3110 cells transformed with the pUA66-*rrnB* plasmid (Zaslaver *et al*, 2006) as a prey. In addition to conferring resistance to kanamycin, the pUA66-*rrnB* plasmid allows a strong constitutive expression of the green fluorescent protein. The experiments were done in triplicate, with identical results, and the results of a representative experiment is shown here.

Co-immunoprecipitation.

W3110 cells producing Tle1, Tle1$_{\Delta 1\text{-}26}$ or VgrG proteins from independent plasmids were subjected to co-immunoprecipitation using ANTI-FLAG® M2 affinity gel (Sigma-Aldrich), as described previously (Flaugnatti *et al*, 2016). Anti-FLAG (clone M2, Sigma-Aldrich) or anti-VSV-G (clone P5D4, Sigma-Aldrich) monoclonal antibodies were used for Western-blot analyses.

VgrG-Tle1 complex production and co-purification.

The pRSF–Tle1^{H} and pET-^{S}VgrG plasmids were co-transformed into BL21(DE3). Following growth at 37°C in LB medium to an OD_{600nm} of 0.7, the expression of *tle1* and *vgrG* genes was induced with 1 mM IPTG at 16°C for 16 h. Cell were pelleted , resuspended in lysis

buffer (50 mM Tris-HCl pH 8.0, 150 mM NaCl, 1 mM EDTA, 100 µg/mL DNase I, 100 µg/mL lysozyme, cOmplete EDTA-free protease inhibitor cocktail (Sigma) and 10 mM $MgCl_2$) and broken using an Emulsiflex-C5 (Avestin). After centrifugation at 38,500 × *g* for 30 min, the supernatant was loaded onto a 5-mL StrepTrap HP column (GE Healthcare) at 4°C and the column was washed with affinity buffer (50 mM Tris-HCl pH 8.0, 150 mM NaCl) at 4°C. The ^{S}VgrG-Tle1^{H} complex was then eluted directly into a 5-mL HisTrap HP (GE Healthcare) column with affinity buffer containing 2.5 mM desthiobiotin (IBA). After a washing step in affinity buffer supplemented with 20 mM imidazole, the ^{S}VgrG-Tle1^{H} complex was eluted in affinity buffer supplemented with 500 mM imidazole. The fractions corresponding to the peak were pooled and loaded onto a Superose 6 10/300 column (GE Healthcare) equilibrated in 50 mM HEPES pH 7.5, 150 mM NaCl buffer. The ^{S}VgrG-Tle1^{H} complex eluted as a single monodisperse peak. The same production conditions and purification protocol were applied for the purification of ^{S}VgrG, ^{S}VgrG$_{1\text{-}490}$, Tle1^{H} and Tle1$_{\Delta 1\text{-}26}$, except that only one affinity column was performed (StrepTrap HP for ^{S}VgrG and ^{S}VgrG$_{1\text{-}490}$, HisTrap for Tle1^{H} and Tle1$_{\Delta 1\text{-}26}$) followed by a gel filtration as described above. For Tle1 inhibition studies, ^{S}VgrG and ^{S}VgrG$_{1\text{-}490}$ eluted from the StrepTrap column were used directly (without a gel filtration step), due to the tendency of ^{S}VgrG to precipitate during or after the gel filtration step when purified alone. A representative SDS-PAGE followed by Instant blue staining of the resulting purified proteins is presented in Fig 5C.

Sypro-Ruby staining.

Aliquots of 2.5, 5, and 10 µL of the VgrG-Tle1 complex from two different peak fractions of the gel filtration column were subjected to SDS-PAGE. The gel was then stained with Sypro-Ruby as recommended by the manufacturer (Invitrogen). Protein bands were visualized using a Biorad Chemidoc MP Imaging system, using a 605/50 Filter (excitation wavelength = 488

nm, emission wavelength = 605 nm) with 0.5 sec exposition, and the fluorescence intensity was quantified using the Fuji Image software. Intensities were divided by the molecular weight of each protein and the quantification is expressed as the mean +/- standard deviation relative to VgrG bands intensity

Cryo-EM sample preparation and data collection

UltraAuFoil Holey gold Film grids (Quantifoil) were glow discharged for 20 s at 2 mA in an ELMO glow discharge cleaning system (Agar Scientific, UK). Four µl of sample at 600 µg/mL were loaded on the glow discharged grid at 100 % humidity and 4°C in a Vitrobot (Thermo Fisher Scientific, USA). Following a 5 s pre-blot the grid was blotted for 4 s and plunged into liquid ethane. Grids were screened on a Talos Arctica electron microscope equipped with a Falcon 3EC camera (Thermo Fisher Scientific, USA), and the final data were collected on a K2-Summit detector through a Gatan Quantum 967 LS energy filter using a 20 eV slit width in zero-loss mode (Gatan, Japan) on a Titan Krios transmission electron microscope at 300 kV (Thermo Fisher Scientific, USA). Table 2 summarises the acquisition parameters.

Cryo-EM data processing

The 40 frames for each movie collected were aligned for each of the 11,600 movies using MotionCor2, binned by 1.28 with dose weighting (1.24 e-/Å2/frame) and with 5 × 5 patches applied (Zheng *et al*, 2017). gCTF was used to estimate the CTF parameters (Zhang, 2016). Cryosparc (Punjani *et al*, 2017) template picker selected 1.94 million particles that were extracted with a box-size of 350 pix. After several rounds of 2D classification in cryosparc (Fig EV2A), a heterogeneous ab initio reconstruction with 2 classes, and a heterogeneous refinement (2 classes), 468,438 particles were selected for homogeneous refinement. An

initial unmasked refinement using the *ab initio* model from the crysoparc *ab initio* class, gave us a resolution of 2.7 Å with no applied symmetry (Fig EV2B-D). A masked local refinement around the physiological complex yielded a final resolution of 2.6 Å (Fig EV2E). The density corresponding to the Tle1 effector was refined locally with cryosparc to a resolution of 2.5 Å. In Relion, CTF Refine and the Bayesian polishing steps (Zivanov *et al*, 2019) yielded a final resolution of 2.3 Å for the masked VgrG density and was used for model building and real space refinement (Fig EV2F and G). The quality of the maps for the Tle1/TTR densities were worse than those obtained with cryosparc and were thus not used. The resolution for the Tle1 and VgrG densities was calculated by cryosparc and Relion postprocess respectively according to the "gold standard" method using 0.143 as the FSC value cut-off (Rosenthal & Henderson, 2003). The local resolution was calculated by cryosparc (Punjani *et al*, 2017) or Relion with a cut-off of 0.5 (Appendix Fig S5A-C).

Model building and validation

Model building proceeded differently for VgrG and Tle1, but for both no homologous protein could be docked in the density and the Phenix autosharpened (Terwilliger *et al*, 2018b) cryo-EM densities were used. For Tle1, a partial initial model based on sequence was built using phenix.map_to_model (Terwilliger *et al*, 2018a). The model was subsequently corrected and extended manually in Coot (Emsley *et al*, 2010). For VgrG, the Phenix automatic model building was not successful. The model was built starting with the only 2 α-helices and using the cryo-EM density to place manually all the amino acid sequence. For the TTR domain that interacts with Tle1, we combined the use of bulky side-chains as guides for model building, secondary structure and residue contact predictions according to the Phyre2 (Kelley *et al*, 2015) and the RaptorX (Källberg *et al*, 2012) servers respectively. The VgrG models were both refined using phenix.real_space_refine (Afonine *et al*, 2018) and manual adjustments were done with Coot (Emsley *et al*, 2010). Each model was initially validated using the

protocol implemented in Refmac5 (Murshudov *et al*, 2011) and visually (Appendix Fig S8). The FSC map-to-model was calculated with the autosharpened maps (FSC_{sum}). The model was shaken by 0.5 Å and the FSC map-to-model was calculated with one Half map (FSC_{work}). This refined model was then used to calculate the FSC map to model with the other Half map (FSC_{free}) (Appendix Fig S8A-C).The cross-correlation between each amino acid in the model and map and the Molprobity score (Chen *et al*, 2010) were calculated using phenix.real_space_refine (Afonine *et al*, 2018) (Appendix Fig S9, Table 2). Pore radius calculations were carried out using the MOLE server (Berka *et al*, 2012) and the protein interfaces were analysed with PISA (Krissinel & Henrick, 2007). Unless stated otherwise, all of the figures were generated either using Chimera (Pettersen *et al*, 2004), ChimeraX (Goddard *et al*, 2018) and Coot (Emsley *et al*, 2010).

Cross-linking mass spectrometry. Cross-linking of the purified complexes was carried out with freshly prepared NNP9 (10 mM in DMSO) using 10:1 cross-linker/protein molar ratio. Cross-linking was performed at 4°C for 30 min and stopped by the addition of ammonium bicarbonate (AB, final concentration 50 mM) for 15 min at 4°C. The samples were transferred into a molecular filter device (Amicon ultra 0.5 mL with 30 KDa molecular cut-off) and centrifuged at 10,000×*g* for 5 min. The concentrate was then washed 4 times by concentration-dilution cycle with AB 50 mM to remove the excess of cross-linker. The labelled protein was digested overnight at 37°C by addition of Trypsin Gold, Mass Spectrometry Grade (Promega) at an enzyme:protein ratio of 1:50 (w:w) under 900 rpm shaking. The peptides were recovered through the molecular filtering device by centrifugation. 50 µL of 0.1% (v:v) formic acid were added onto the filter and a second centrifugation was performed to improve the peptide recovery. Cross-linked protein digests were analyzed by nanoLC-MS/MS on an Orbitrap Q Exactive Plus mass spectrometer

(Thermo-Scientific). Briefly, peptides were separated on homemade C18 column using a 90 min water/acetonitrile gradient. The 10 most intense ions with at least 3 charges were selected for HCD fragmentation (NCE 24). NanoLC-MS/MS data were processed automatically using Mass Spec Studio v2.0 (Sarpe *et al*, 2016) with methionine oxidation as a variable modification and NNP9 modification sites: lysine, serine, threonine, and tyrosine. Mass modifications were set to 314.1127 Da for cross-linked peptides, 288.1335 and 331.1393 for dead-end modifications when NNP9 reacted respectively with water or ammonium molecule. Cross-linked peptides were searched using the parameter file provided in supplemental data (Dataset EV2). MS/MS spectra of all crosslinked candidates were further manually checked to confirm their identification. Experiments were performed in duplicate (using two different complex preparations) and only cross-linked peptides identified in both experiments were considered.

Phospholipase A_1 fluorescent assays.

PLA1 activities of Tle1, $Tle1_{\Delta 1\text{-}26}$, VgrG and the VgrG-Tle1 complex were monitored using BODIPYVR dye-labeled phospholipids: PED-A1(N-((6-(2,4-DNP)Amino)Hexanoyl)-(BODIPYVRFL C5)-2-Hexyl-sn-Glycero-3-Phosphoethanolamine (Farber, 2001; Darrow *et al*, 2011), as described previously (Flaugnatti *et al*, 2016). Enzyme activities were assayed at room temperature in 50 mM HEPES pH 7.5, 150 mM NaCl for 25 min in a final volume of 200 µL containing 5 µM of the substrate and 1.18 µM of $Tle1^{H}$, 1.18 µM of ^{S}VgrG or 0.393 µM of ^{S}VgrG-$Tle1^{H}$ complex (corresponding to 1.18 µM of Tle1 considering a 3:3 stoichiometry) purified proteins (from 1-2 mg/mL stock solutions). *Thermomyces lanuginosus* lipase (TLL, Sigma-Aldrich) was used as a positive control for PLA1 activity. Inhibition assays were performed in desthiobiotin containing buffer (Tris-HCl 50 mM pH 8.0, NaCl 150 mM, desthiobiotin 2.5 mM) using ^{S}VgrG or $^{S}VgrG_{1\text{-}490}$ purified at 1.5-2 mg/mL, after

checking that desthiobiotin did not affect Tle1 PLA1 activity. Lysozyme from chicken egg white (Sigma) was used as a negative control. Differences in Tle1 activities between groups were examined by unpaired two-sample Fisher-Pitman permutation test.

Computer algorithms.

EAEC Tle1 orthologs (EC042_4534; NCBI Gene Identifier (GI): 284924255) were detected using BlastP analysis against the KEGG genes database and aligned using ClustalW and draw alignment tool in KEGG (Kanehisa *et al*, 2017), or Multialin (Corpet, 1988; Robert & Gouet, 2014) Protein domains were identified using Pfam (Sonnhammer *et al*, 1997) or CDart (Geer, 2002).

Data availability

Electron microscopy maps of VgrG-Tle1, VgrG and Tle1-TTR complexes have been deposited in the Electron Microscopy Databank (EMDB) and the PDB under accession codes EMD-10218 (PDB 6SJL), EMD-10219 (PDB 6SK0) and EMD-10225 (PDB 6SKI) respectively.

Acknowledgements

We thank the members of the Cascales, Lloubès, Bouveret and Sturgis groups for discussions, Artemis Kosta for EM assistance, Moly Ba, Isabelle Bringer, Annick Brun and Olivier Uderso for technical assistance. This work has benefitted from the facilities and expertise of the Biophysical and Structural Chemistry platform (BPCS) at IECB, CNRS UMS3033, Inserm US001, Bordeaux University, in particular we would like to thank Armel Bezault. The authors acknowledge the use of resources of the cryo-electron microscopy service platform at the EMBL Heidelberg and the support of Felix Weis for data collection. The access to the facility

561 has been supported by iNEXT, grant number 653706, funded by the Horizon 2020
562 programme of the European Commission.

563 This work was supported by the Centre National de la Recherche Scientifique (CNRS), Aix-
564 Marseille Université and grants from the Agence Nationale de la Recherche (ANR-14-CE14-
565 0006-02 and ANR-18-CE15-0013-01). NF was supported by the ANR-14-CE14-0006-02
566 grant. The work of ED is supported by the Institut National de la Santé et de la Recherche
567 Médicale (INSERM). The work of MR is supported by the Institut Pasteur, the CNRS and the
568 Projet d'Investissement d'Avenir BIP:BIP (ANR-10-BINF-03-13).

569 **Author contributions**

570 NF, CR, MR, ED, JCR, RF & LJ designed research. NF, CR, MR, SGB, VAN & LJ
571 performed research. MR, SC, JCR, RF & EC provided tools. NF, CR, MR, SGB, ED, SC, EC,
572 RF & LJ analyzed data. NF, CR, RF & LJ wrote the paper with contributions of MR, JCR &
573 EC.

574 **Conflict of Interests**

575 The authors declare that they have no conflict of interest.

576

577 **REFERENCES**

578

579 Afonine P V., Poon BK, Read RJ, Sobolev O V., Terwilliger TC, Urzhumtsev A & Adams
580 PD (2018) Real-space refinement in PHENIX for cryo-EM and crystallography. *Acta*
581 *Crystallogr*. *Sect*. *D Struct*. *Biol*. **74:** 531–544

582 Alcoforado Diniz J & Coulthurst SJ (2015) Intraspecies Competition in Serratia marcescens Is

583 Mediated by Type VI-Secreted Rhs Effectors and a Conserved Effector-Associated
584 Accessory Protein. *J*. *Bacteriol*. **197:** 2350–2360

585 Basler M, Pilhofer M, Henderson GP, Jensen GJ & Mekalanos JJ (2012) Type VI secretion
586 requires a dynamic contractile phage tail-like structure. *Nature* **483:** 182–186

587 Berka K, Hanak O, Sehnal D, Banas P, Navratilova V, Jaiswal D, Ionescu C-M, Svobodova
588 Varekova R, Koca J & Otyepka M (2012) MOLEonline 2.0: interactive web-based
589 analysis of biomacromolecular channels. *Nucleic Acids Res*. **40:** W222–W227

590 Blondel CJ, Jiménez JC, Contreras I & Santiviago CA (2009) Comparative genomic analysis
591 uncovers 3 novel loci encoding type six secretion systems differentially distributed in
592 Salmonella serotypes. *BMC Genomics* **10:** 354

593 Bondage DD, Lin J-S, Ma L-S, Kuo C-H & Lai E-M (2016) VgrG C terminus confers the
594 type VI effector transport specificity and is required for binding with PAAR and
595 adaptor–effector complex. *Proc*. *Natl*. *Acad*. *Sci*. **113:** E3931–E3940

596 Boyer F, Fichant G, Berthod J, Vandenbrouck Y & Attree I (2009) Dissecting the bacterial
597 type VI secretion system by a genome wide in silico analysis: what can be learned from
598 available microbial genomic resources? *BMC Genomics* **10:** 104

599 Brooks TM, Unterweger D, Bachmann V, Kostiuk B & Pukatzki S (2013) Lytic Activity of
600 the Vibrio cholerae Type VI Secretion Toxin VgrG-3 Is Inhibited by the Antitoxin TsaB.
601 *J*. *Biol*. *Chem*. **288:** 7618–7625

602 Brunet YR, Bernard CS, Gavioli M, Lloubès R & Cascales E (2011) An Epigenetic Switch
603 Involving Overlapping Fur and DNA Methylation Optimizes Expression of a Type VI
604 Secretion Gene Cluster. *PLoS Genet*. **7:** e1002205

605 Brunet YR, Zoued A, Boyer F, Douzi B & Cascales E (2015) The Type VI Secretion
606 TssEFGK-VgrG Phage-Like Baseplate Is Recruited to the TssJLM Membrane Complex

via Multiple Contacts and Serves As Assembly Platform for Tail Tube/Sheath Polymerization. *PLOS Genet*. **11:** e1005545

Chen VB, Arendall WB, Headd JJ, Keedy DA, Immormino RM, Kapral GJ, Murray LW, Richardson JS & Richardson DC (2010) MolProbity : all-atom structure validation for macromolecular crystallography. *Acta Crystallogr*. *Sect*. *D Biol*. *Crystallogr*. **66:** 12–21

Cherrak Y, Rapisarda C, Pellarin R, Bouvier G, Bardiaux B, Allain F, Malosse C, Rey M, Chamot-Rooke J, Cascales E, Fronzes R & Durand E (2018) Biogenesis and structure of a type VI secretion baseplate. *Nat*. *Microbiol*. **3:** 1404–1416

Cianfanelli FR, Monlezun L & Coulthurst SJ (2016) Aim, Load, Fire: The Type VI Secretion System, a Bacterial Nanoweapon. *Trends Microbiol*. **24:** 51–62

Corpet F (1988) Multiple sequence alignment with hierarchical clustering. *Nucleic Acids Res*. **16:** 10881–10890

Darrow AL, Olson MW, Xin H, Burke SL, Smith C, Schalk-Hihi C, Williams R, Bayoumy SS, Deckman IC, Todd MJ, Damiano BP & Connelly MA (2011) A novel fluorogenic substrate for the measurement of endothelial lipase activity. *J*. *Lipid Res*. **52:** 374–382

Dong TG, Ho BT, Yoder-Himes DR & Mekalanos JJ (2013) Identification of T6SS-dependent effector and immunity proteins by Tn-seq in Vibrio cholerae. *Proc*. *Natl*. *Acad*. *Sci*. **110:** 2623–2628

Durand E, Cambillau C, Cascales E & Journet L (2014) VgrG, Tae, Tle, and beyond: the versatile arsenal of Type VI secretion effectors. *Trends Microbiol*. **22:** 498–507

Durand E, Nguyen VS, Zoued A, Logger L, Péhau-Arnaudet G, Aschtgen M-S, Spinelli S, Desmyter A, Bardiaux B, Dujeancourt A, Roussel A, Cambillau C, Cascales E & Fronzes R (2015) Biogenesis and structure of a type VI secretion membrane core complex. *Nature* **523:** 555–560

631 Emsley P, Lohkamp B, Scott WG & Cowtan K (2010) Features and development of Coot.
632 *Acta Crystallogr*. *Sect*. *D Biol*. *Crystallogr*. **66:** 486–501

633 Farber SA (2001) Genetic Analysis of Digestive Physiology Using Fluorescent Phospholipid
634 Reporters. *Science (80-.)*. **292:** 1385–1388

635 Flaugnatti N, Le TTH, Canaan S, Aschtgen M-S, Nguyen VS, Blangy S, Kellenberger C,
636 Roussel A, Cambillau C, Cascales E & Journet L (2016) A phospholipase A 1
637 antibacterial Type VI secretion effector interacts directly with the C-terminal domain of
638 the VgrG spike protein for delivery. *Mol*. *Microbiol*. **99:** 1099–1118

639 Geer LY, Domrachev M, Lipman DJ & Bryant SH (2002) CDART: Protein Homology by
640 Domain Architecture. *Genome Res*. **12:** 1619–1623

641 Goddard TD, Huang CC, Meng EC, Pettersen EF, Couch GS, Morris JH & Ferrin TE (2018)
642 UCSF ChimeraX: Meeting modern challenges in visualization and analysis. *Protein Sci*.
643 **27:** 14–25

644 Guzman LM, Belin D, Carson MJ & Beckwith J (1995) Tight regulation, modulation, and
645 high-level expression by vectors containing the arabinose PBAD promoter. *J*. *Bacteriol*.
646 **177:** 4121–4130

647 Hachani A, Wood TE & Filloux A (2016) Type VI secretion and anti-host effectors. *Curr*.
648 *Opin*. *Microbiol*. **29:** 81–93

649 Ho BT, Dong TG & Mekalanos JJ (2014) A View to a Kill: The Bacterial Type VI Secretion
650 System. *Cell Host Microbe* **15:** 9–21

651 Hu H, Zhang H, Gao Z, Wang D, Liu G, Xu J, Lan K & Dong Y (2014) Structure of the type
652 VI secretion phospholipase effector Tle1 provides insight into its hydrolysis and
653 membrane targeting. *Acta Crystallogr*. *Sect*. *D Biol*. *Crystallogr*. **70:** 2175-2185

654 Källberg M, Wang H, Wang S, Peng J, Wang Z, Lu H & Xu J (2012) Template-based protein

structure modeling using the RaptorX web server. *Nat*. *Protoc*. **7:** 1511–1522

Kanamaru S, Leiman PG, Kostyuchenko VA, Chipman PR, Mesyanzhinov V V., Arisaka F & Rossmann MG (2002) Structure of the cell-puncturing device of bacteriophage T4. *Nature* **415:** 553–557

Kanehisa M, Furumichi M, Tanabe M, Sato Y & Morishima K (2017) KEGG: new perspectives on genomes, pathways, diseases and drugs. *Nucleic Acids Res*. **45:** D353–D361

Kelley LA, Mezulis S, Yates CM, Wass MN & Sternberg MJE (2015) The Phyre2 web portal for protein modeling, prediction and analysis. *Nat*. *Protoc*. **10:** 845–858

Krissinel E & Henrick K (2007) Inference of Macromolecular Assemblies from Crystalline State. *J*. *Mol*. *Biol*. **372:** 774–797

Leiman PG, Basler M, Ramagopal UA, Bonanno JB, Sauder JM, Pukatzki S, Burley SK, Almo SC & Mekalanos JJ (2009) Type VI secretion apparatus and phage tail-associated protein complexes share a common evolutionary origin. *Proc*. *Natl*. *Acad*. *Sci*. **106:** 4154–4159

Liang X, Moore R, Wilton M, Wong MJQ, Lam L & Dong TG (2015) Identification of divergent type VI secretion effectors using a conserved chaperone domain. *Proc*. *Natl*. *Acad*. *Sci*. **112:** 9106–9111

Logger L, Aschtgen M-S, Guérin M, Cascales E & Durand E (2016) Molecular Dissection of the Interface between the Type VI Secretion TssM Cytoplasmic Domain and the TssG Baseplate Component. *J*. *Mol*. *Biol*. **428:** 4424–4437

Ma J, Pan Z, Huang J, Sun M, Lu C & Yao H (2017) The Hcp proteins fused with diverse extended-toxin domains represent a novel pattern of antibacterial effectors in type VI secretion systems. *Virulence* **8:** 1189–1202

679 Murshudov GN, Skubák P, Lebedev AA, Pannu NS, Steiner RA, Nicholls RA, Winn MD,
680 Long F & Vagin AA (2011) REFMAC 5 for the refinement of macromolecular crystal
681 structures. *Acta Crystallogr*. *Sect*. *D Biol*. *Crystallogr*. **67:** 355–367

682 Nazarov S, Schneider JP, Brackmann M, Goldie KN, Stahlberg H & Basler M (2018) Cryo-
683 EM reconstruction of Type VI secretion system baseplate and sheath distal end. *EMBO*
684 *J*. **37:** e97103

685 Nguyen VS, Logger L, Spinelli S, Legrand P, Huyen Pham TT, Nhung Trinh TT, Cherrak Y,
686 Zoued A, Desmyter A, Durand E, Roussel A, Kellenberger C, Cascales E & Cambillau C
687 (2017) Type VI secretion TssK baseplate protein exhibits structural similarity with phage
688 receptor-binding proteins and evolved to bind the membrane complex. *Nat*. *Microbiol*. **2:**
689 17103

690 Nury C, Redeker V, Dautrey S, Romieu A, van der Rest G, Renard P-Y, Melki R & Chamot-
691 Rooke J (2015) A Novel Bio-Orthogonal Cross-Linker for Improved Protein/Protein
692 Interaction Analysis. *Anal*. *Chem*. **87:** 1853–1860

693 Pettersen EF, Goddard TD, Huang CC, Couch GS, Greenblatt DM, Meng EC & Ferrin TE
694 (2004) UCSF Chimera--a visualization system for exploratory research and analysis. *J*.
695 *Comput*. *Chem*. **25:** 1605–12

696 Pukatzki S, Ma AT, Sturtevant D, Krastins B, Sarracino D, Nelson WC, Heidelberg JF &
697 Mekalanos JJ (2006) Identification of a conserved bacterial protein secretion system in
698 *Vibrio cholerae* using the *Dictyostelium* host model system. *Proc*. *Natl*. *Acad*. *Sci*. *U*. *S*.
699 *A*. **103:** 1528–1533

700 Punjani A, Rubinstein JL, Fleet DJ & Brubaker MA (2017) cryoSPARC: algorithms for rapid
701 unsupervised cryo-EM structure determination. *Nat*. *Methods* **14:** 290–296

702 Quentin D, Ahmad S, Shanthamoorthy P, Mougous JD, Whitney JC & Raunser S (2018)

Mechanism of loading and translocation of type VI secretion system effector Tse6. *Nat*. *Microbiol*. **3:** 1142–1152

Rapisarda C, Cherrak Y, Kooger R, Schmidt V, Pellarin R, Logger L, Cascales E, Pilhofer M, Durand E & Fronzes R (2019) In situ and high-resolution cryo- EM structure of a bacterial type VI secretion system membrane complex. *EMBO J*. **38:** e100886

Robert X & Gouet P (2014) Deciphering key features in protein structures with the new ENDscript server. *Nucleic Acids Res*. **42:** W320–W324

Rosenthal PB & Henderson R (2003) Optimal Determination of Particle Orientation, Absolute Hand, and Contrast Loss in Single-particle Electron Cryomicroscopy. *J*. *Mol*. *Biol*. **333:** 721–745

Russell AB, Peterson SB & Mougous JD (2014) Type VI secretion system effectors: Poisons with a purpose. *Nat*. *Rev*. *Microbiol*. **12:** 137–148

Sarpe V, Rafiei A, Hepburn M, Ostan N, Schryvers AB & Schriemer DC (2016) High Sensitivity Crosslink Detection Coupled With Integrative Structure Modeling in the Mass Spec Studio. *Mol*. *Cell*. *Proteomics* **15:** 3071–3080

Shneider MM, Buth SA, Ho BT, Basler M, Mekalanos JJ & Leiman PG (2013) PAAR-repeat proteins sharpen and diversify the type VI secretion system spike. *Nature* **500:** 350–353

Silverman JM, Agnello DM, Zheng H, Andrews BT, Li M, Catalano CE, Gonen T & Mougous JD (2013) Haemolysin Coregulated Protein Is an Exported Receptor and Chaperone of Type VI Secretion Substrates. *Mol*. *Cell* **51:** 584–593

Sonnhammer ELL, Eddy SR & Durbin R (1997) Pfam: A comprehensive database of protein domain families based on seed alignments. *Proteins Struct*. *Funct*. *Genet*. **28:** 405–420

Spínola-Amilibia M, Davó-Siguero I, Ruiz FM, Santillana E, Medrano FJ & Romero A (2016) The structure of VgrG1 from Pseudomonas aeruginosa , the needle tip of the

727 bacterial type VI secretion system. *Acta Crystallogr*. *Sect*. *D Struct*. *Biol*. **72:** 22–33

728 Suarez G, Sierra JC, Erova TE, Sha J, Horneman AJ & Chopra AK (2010) A type VI
729 secretion system effector protein, VgrG1, from Aeromonas hydrophila that induces host
730 cell toxicity by ADP ribosylation of actin. *J*. *Bacteriol*. **192:** 155–168

731 Taylor NMI, Prokhorov NS, Guerrero-Ferreira RC, Shneider MM, Browning C, Goldie KN,
732 Stahlberg H & Leiman PG (2016) Structure of the T4 baseplate and its function in
733 triggering sheath contraction. *Nature* **533:** 346–352

734 Terwilliger TC, Adams PD, Afonine P V. & Sobolev O V. (2018a) A fully automatic method
735 yielding initial models from high-resolution cryo-electron microscopy maps. *Nat*.
736 *Methods* **15:** 905–908

737 Terwilliger TC, Sobolev O V., Afonine P V. & Adams PD (2018b) Automated map
738 sharpening by maximization of detail and connectivity. *Acta Crystallogr*. *Sect*. *D Struct*.
739 *Biol*. **74:** 545–559

740 Uchida K, Leiman PG, Arisaka F & Kanamaru S (2014) Structure and properties of the C-
741 terminal β-helical domain of VgrG protein from Escherichia coli O157. *J*. *Biochem*. **155:**
742 173–182

743 Unterweger D, Kostiuk B, Otjengerdes R, Wilton A, Diaz-Satizabal L & Pukatzki S (2015)
744 Chimeric adaptor proteins translocate diverse type VI secretion system effectors in
745 Vibrio cholerae. *EMBO J*. **34:** 2198–2210

746 Vieira J & Messing J (1991) New pUC-derived cloning vectors with different selectable
747 markers and DNA replication origins. *Gene* **100:** 189–94

748 Wettstadt S, Wood TE, Fecht S & Filloux A (2019) Delivery of the Pseudomonas aeruginosa
749 Phospholipase Effectors PldA and PldB in a VgrG- and H2-T6SS-Dependent Manner.
750 *Front*. *Microbiol*. **10:** 1718

751 Whitney JC, Quentin D, Sawai S, LeRoux M, Harding BN, Ledvina HE, Tran BQ, Robinson
752 H, Goo YA, Goodlett DR, Raunser S & Mougous JD (2015) An Interbacterial NAD(P)+
753 Glycohydrolase Toxin Requires Elongation Factor Tu for Delivery to Target Cells. *Cell*
754 **163:** 607–619

755 Wood TE, Howard SA, Wettstadt S & Filloux A (2019) PAAR proteins act as the 'sorting
756 hat' of the type VI secretion system. *Microbiology* **165:** 1203–1218

757 Zaslaver A, Bren A, Ronen M, Itzkovitz S, Kikoin I, Shavit S, Liebermeister W, Surette MG
758 & Alon U (2006) A comprehensive library of fluorescent transcriptional reporters for
759 Escherichia coli. *Nat*. *Methods* **3:** 623–8

760 Zhang K (2016) Gctf: Real-time CTF determination and correction. *J*. *Struct*. *Biol*. **193:** 1–12

761 Zheng SQ, Palovcak E, Armache J-P, Verba KA, Cheng Y & Agard DA (2017) MotionCor2:
762 anisotropic correction of beam-induced motion for improved cryo-electron microscopy.
763 *Nat*. *Methods* **14:** 331–332

764 Zivanov J, Nakane T & Scheres SHW (2019) A Bayesian approach to beam-induced motion
765 correction in cryo-EM single-particle analysis. *IUCrJ* **6:** 5–17

766 Zoued A, Brunet YR, Durand E, Aschtgen MS, Logger L, Douzi B, Journet L, Cambillau C &
767 Cascales E (2014) Architecture and assembly of the Type VI secretion system. *Biochim*.
768 *Biophys*. *Acta - Mol*. *Cell Res*. **1843:** 1664–1673

769 Zoued A, Durand E, Brunet YR, Spinelli S, Douzi B, Guzzo M, Flaugnatti N, Legrand P,
770 Journet L, Fronzes R, Mignot T, Cambillau C & Cascales E (2016) Priming and
771 polymerization of a bacterial contractile tail structure. *Nature* **531:** 59–63

772

773

FIGURE LEGENDS

Figure 1. The N-terminal extension of Tle1 is required for VgrG-mediated transport into target cells.

A. Cross-link connectivity map of ^{S}VgrG-Tle1^{H} complex. The two proteins are represented as rectangles in which the residues number and known domains are indicated. Straight lines represent inter-molecular cross-links, while dotted lines represent intra-molecular cross-links. Only the cross-links identified in two independent experiments were considered. Raw and cured data are provided in Dataset EV1.

B. Schematic representation of an alignment of Tle1 orthologs using ClustalW and draw alignment tool in KEGG (Kanehisa *et al*, 2017). Red box, bit score ≥ 200; pink box, bit score ≥ 80-200. Ordered locus names of the identified genes are indicated on the right. Domains are represented in grey boxes (Hcp, PF05638; PAAR (P), PF05488; VgrG, PF05954, COG3501; DUF2345, PF10106). The N-terminal segment found in EAEC Tle1 protein and absent in the others is represented by a blue box.

C. Antibacterial competition assay. *E. coli* K12 recipient cells (W3110 *gfp*$^{+}$, *kan*^{R}) were mixed with the indicated EAEC attacker cells (1:4 ratio): WT, ΔT6SS-1 and Δ*tle1-tli1* carrying pBAD18 and pBAD33 vectors, or producing the indicated proteins, and spotted on SIM 0.02 % arabinose agar plates for 4-h at 37°C. The image of the corresponding representative bacterial spots is presented and the number of recovered prey cells is indicated in the upper graph (in log of colony-forming units (cfu)). The black, dark grey and light grey circles indicate values obtained from three different spots, and the average is indicated by the bar. Western blot analysis of the production of Tle1$_{V}$ and Tle1$_{\Delta 1\text{-}26\ V}$ is shown in the inset. The experiment was performed in triplicate and a representative result is shown.

D. Co-immunoprecipitation assay. Lysates from *E. coli* K-12 W3110 cells producing VSVG-tagged Tle1 ($Tle1_V$) or VSVG-tagged $Tle1_{\Delta 1\text{-}26}$ truncated variant ($Tle1_{\Delta 1\text{-}26\ V}$) were mixed with lysates from W3110 cells producing FLAG-tagged VgrG ($VgrG_{FL}$) or not (-, empty vector) and subjected to immunoprecipitation on anti-FLAG-coupled beads. The mixed soluble lysates (Input) and the immunoprecipitated material (IP) were subjected to 12.5% SDS-PAGE and immunodetected with anti-FLAG (upper panel) and anti-VSVG (lower panel) monoclonal antibodies. Molecular weight markers (in kDa) are indicated on the left. This experiment was performed in triplicate and a representative result is shown.

Figure 2. ~~Figure 3~~ Cryo-EM density and pseudoatomic model of the VgrG needle (491-834) bound to Tle1.

A-C. Autosharpened and masked cryo-EM density (Level 0.728) of the physiological complex in different orientations

D-F. Ribbon diagram of the VgrG and Tle1 pseudoatomic structure, coloured according to the chain and in different orientations

G. Full VgrG structure composed of the experimentally-obtained spike (red) and the homology model of the base (dark red)

H. Structure of the VgrG spike at different planes

Figure 3. Tle1 structure and interaction with VgrG.

A-B. Ribbon representation of the Tle1 pseudoatomic model. Strands are in pink and helices in light blue. The inset shows the catalytic triad.

C-E. Ribbon representation of the interaction site between the Tle1 finger domain in yellow green and the VgrG TTR domain in red. The site is shown in different orientations.

F-H. Molecular surface representation of the interactions between Tle1 chain D and chains A-C of VgrG respectively (**F**, **G** and **H**).

Figure 4. ~~Supplementary Figure 10~~. Comparison of the active site of Tle1.

A-B. Surface representation and cross section of Tle1 from *P. aeruginosa* (PDB 4O5P) (**A**) and EAEC - this study (**B**). The active site is shown in red. The substrate entry channel is indicated when present.

Figure 5. Inhibition of Tle1 by VgrG.

A. Specific phospholipase A_1 (PLA1) activity measurements of $Tle1^H$, ^SVgrG-$Tle1^H$ complex, and isolated ^SVgrG. *Thermomyces lanuginosus* lipase (TLL) was used as positive standard for PLA1 activity. Mean values and standard deviation from at least three independent assays are shown. Statistical analysis relative to the Tle1 activity is indicated. ***P<0.001 (P=0,0001998), unpaired two-sample Fisher-Pitman permutation test.

B. VgrG inhibition of $Tle1^H$. Specific phospholipase A_1 (PLA1) activity measurements of purified $Tle1^H$ in the presence of 1:10 molar ratio of lysozyme from chicken egg white (Lyso) and increasing molar ratio (0, 1, 5, and 10) of ^SVgrG or $^SVgrG_{1\text{-}490}$. Inhibition experiments with ^SVgrG were repeated three times with independent protein preparations, each measured in triplicate. Inhibition experiments with $^SVgrG_{1\text{-}490}$ were repeated twice with two independent protein preparations, each measured in triplicate. Mean values and standard deviation are shown. Statistical analysis relative to the Tle1 activity is indicated. ns, non-significant (P>0.05), **P<0.01, ***P<0.001, unpaired two-sample Fisher-Pitman permutation test. (P values: Lyso, 0.7006; VgrG 1:1, 0.004946; VgrG 1:5, 1.448e-07; VgrG1:10, 1.448e-07; $VgrG_{1\text{-}490}$ 1:1, 0.5627; $VgrG_{1\text{-}490}$ 1:5, 0.2977; $VgrG_{1\text{-}490}$ 1:10, 0.002631).

C. Representative SDS-PAGE / Coomassie blue staining of the Tle1^{H}, ^{S}VgrG and ^{S}VgrG$_{1\text{-}490}$ purified proteins used in (**B)** (5 µg/well).

INTERACTION	H-BONDS	SALT BRIDGES
A-D	A.K596-D.F257	A.R592-D.E508
	A.K596-D.N260	
	A.Q612-D.D503	
	A.Q605-D.R513	
B-D		B.E513-D.R393
		B.D657-D.K517
C-D	C.G522-D.N390	
	C.E520-D.R393	
TTR-TLE1	G778-S17	D785-K29
	I782- V25	R797-D228
	I782- K23	
	T784- V25	
	S825- H14	
	V826-H14	
	K828-A12	

872
873 **Table 1. Interacting amino acids between VgrG and Tle1 as determined by PISA**
874 **software**
875

876

877

878

879

880

881

882

883

884

885

886

887

888

889

	VgrG-Tle (EMD-10218) (PDB 6SJL)	VgrG (EMD-10219) (PDB 6SK0)	Tle-TTR (EMD-10225) (PDB 6SKI)
Data collection and processing			
Magnification	165,000X	165,000X	165,000X
Voltage (kV)	300	300	300
Electron exposure (e–/Å^2)	53.94	53.94	53.94
Defocus range (μm)	0.5 to 2	0.5 to 2	0.5 to 2
Pixel size (Å)	0.85	0.85	0.85
Spot size	9	9	9
Symmetry imposed	C1	C1	C1
Number of images	11,670	11,670	11,670
Initial particle images (no.)	1,942,084	1,942,084	1,942,084
Final particle images (no.)	468,438	468,438	468,438
Map resolution (Å)	2.6 (2.9)	2.26 (2.7)	2.55 (2.8)
FSC threshold	0.143 (0.5)	0.143 (0.5)	0.143 (0.5)
Map resolution range (Å)	2.2-15	2.15-2.48	2.25-7
Binning	1.28	1.28	1.28
Refinement			
Initial model used (PDB code)	N/A	N/A	N/A
Model resolution (Å)	2.6 (2.7)	2.1 (2.2)	2.6 (2.7)
FSC threshold	0.143 (0.5)	0.143 (0.5)	0.143 (0.5)
Map sharpening *B* factor (Å^2)	84.99	66.07	75.21
Model composition:			
Number of chains	6	3	2
Non-hydrogen atoms	19460	5890	4434
Protein residues	2537	801	569
Ligands	0	0	0
B factors (Å^2):			
Protein (min/max)	25.27/157.57	34.83/63.05	40.72/92.41
Ligand	N/A	N/A	N/A
R.m.s. deviations:			
Bond lengths (Å)	0.013	0.008	0.004
Bond angles (°)	0.855	0.726	0.713
Validation:			
MolProbity score	2.02	1.70	1.55
Clashscore	12.96	9.23	8.64
Poor rotamers (%)	0.05	0.97	1.29
Ramachandran plot:			
Favoured (%)	94.06	96.69	98.38
Allowed (%)	5.74	3.31	1.62
Disallowed (%)	0.20	0	0

890 **Table 2. Cryo-EM data acquisition and analysis parameters**

891

EXPANDED VIEW FIGURE LEGENDS

Figure EV1. Purification and biochemical characterization of the VgrG-Tle1 complex

A. SDS–PAGE analysis and Coomassie staining (upper panel) or immunoblotting using anti-StrepII (middle panel) and anti-His (lower panel) antibodies of the ^{S}VgrG-Tle1^{H} complex purification steps. Lysate of cells (L) co-producing StrepII-VgrG (^{S}VgrG) and Tle1-6×His (Tle1^{H}) was loaded on a StrepTrap HP column. After washing (W), the material eluted with desthiobiotin was directed loaded on a HisTrap column. The material eluted with imidazole (E) was pooled and loaded on a Superose 6 10/300 gel filtration (GF) column. Ten microliters of each fraction were loaded on the gel. Molecular weight markers in kDa and the positions of ^{S}VgrG and Tle1^{H} are indicated on the left and right, respectively. FT, flow through.

B. Size-exclusion chromatography analysis of the purified ^{S}VgrG-Tle1^{H} complex (blue line) and of purified ^{S}VgrG alone (Appendix Fig S1) was performed on a Superose 6 column calibrated with 43-, 75-, 158-, 440- and 660-kDa molecular mass markers (dotted lines). The molecular mass of each marker and the position of the peak fractions corresponding to ^{S}VgrG-Tle1^{H} and ^{S}VgrG is indicated at the top of each peak.

C. SYPRO Ruby staining analysis of the ^{S}VgrG-Tle1^{H} complex. The indicated volumes of two different fractions corresponding to the center of the gel filtration peak were subjected to SDS-PAGE and stained with SYPRO Ruby. Fluorescence intensities were divided by the molecular weight of each protein and the quantification is expressed as the mean (+/- SD) relative to VgrG.

Figure EV2. Data analysis of the VgrG-Tle1 structure

A. 2D classes of the VgrG-Tle1 complex representative of all the orientations observed. The number of particles and the resolution reached during classification are indicated in green.

B-C. Sharpened cryo-EM density of the full complex in two different orientations.

D-G. Gold standard FSC curves of the Full complex (**D**), the VgrG-Tle1 complex (**E**), VgrG alone (**F**) and Tle1 with the TTR domain (**G**). For (**D**, **E** and **G)** the colours indicate the FSC curves without mask (blue), spherical mask (green), loose mask (grey) and tight mask (orange) applied. For (**F)**, the colours indicate the FSC curves that were corrected (blue), unmasked (green), masked (grey) and phase randomised (orange).

Figure EV3. VgrG structure and mechanism of effector loading.

A-C. Ribbon diagrams of 1 chain of VgrG from (**A**) EAEC, (**B**) *P*. *aeruginosa* (4MTK), and (**C**) gp5 from the T4 phage (1K28).

D-F. Ribbon diagrams of the spike complexes with their effector from (**D**) EAEC, (**E**) *P*. *aeruginosa* (PDB 6H3L), and (**F**) the $(gp27)_3$-$(gp5)_3$ complex from the T4 phage (1K28). The cryo-EM densities (EMD-0135 for PA) of the VgrG proteins with their effectors are shown with 20% transparency.

Figure EV4. Tle1 structure.

A. Topology diagram of Tle1 adapted from the output of PDBsum. The helices are in blue and the strands are in pink, as in Fig 3. The catalytic amino acids and the domains relevant to Tle1 structure are highlighted.

B-C. Ribbon diagram of the pseudoatomic structure of Tle1 and the TTR domain of VgrG coloured according to B-factors. Blue = 34, White = 65 and Red = 96.

Figure EV5. ~~Supplementary Figure 9~~. Analysis of the Tle1 active site.

A. Ribbon diagram of Tle1 with the active site and the pore leading to the catalytic amino acids highlighted.

B. Cross-section of the active site entrance channel of Tle1, coloured according to its charge, as calculated with the APBS server.

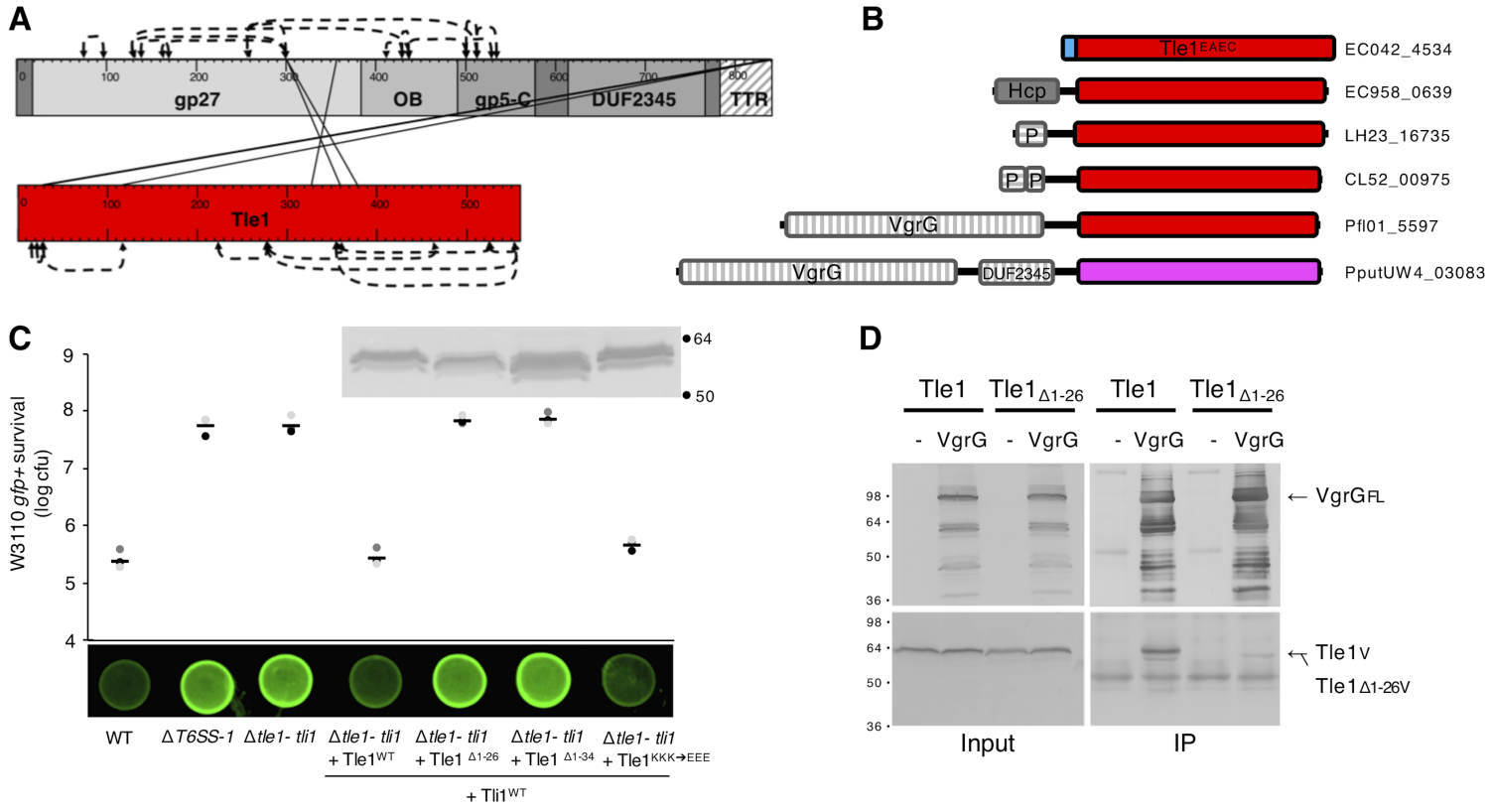
A
gp27
OB
gp5-C
DUF2345
TTR
Tle1
B
Tle1EAEC
EC042_4534
Hcp
EC958_0639
P
LH23_16735
P P
CL52_00975
VgrG
Pfl01_5597
VgrG
DUF2345
PputUW4_03083
C
W3110 gfp+ survival (log cfu)
64
50
WT
ΔT6SS-1
Δtle1- tli1
Δtle1- tli1 + Tle1WT
Δtle1- tli1 + Tle1 Δ1-26
Δtle1- tli1 + Tle1 Δ1-34
Δtle1- tli1 + Tle1KKK→EEE
+ Tli1WT
D
Tle1
Tle1Δ1-26
- VgrG
VgrGFL
Tle1V
Tle1Δ1-26V
Input
IP

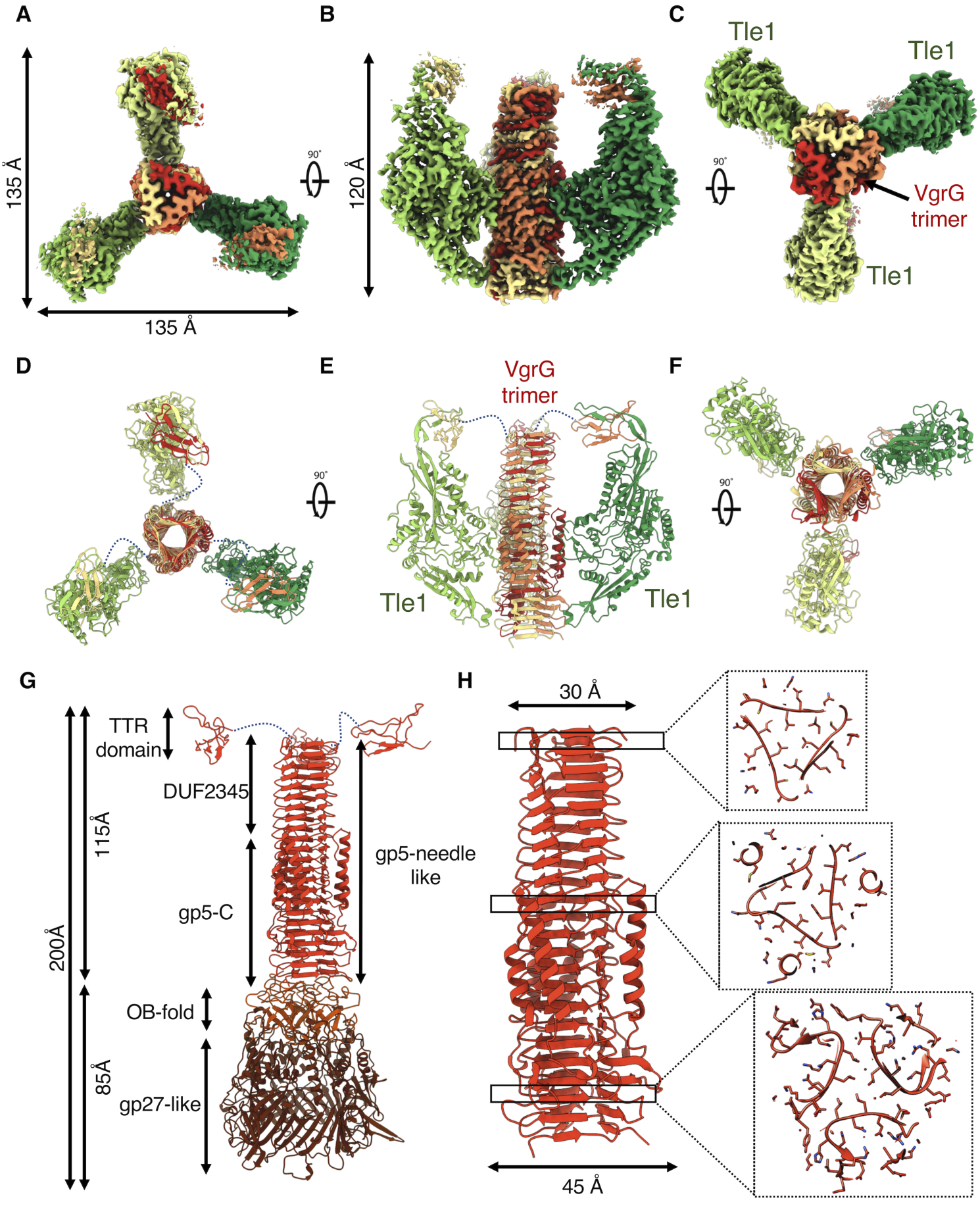
A
135 Å
135 Å
90˚
B
120 Å
C
Tle1
Tle1
90˚
VgrG
trimer
Tle1
D
90˚
E
VgrG
trimer
Tle1
Tle1
F
90˚
G
TTR
domain
DUF2345
gp5-C
gp5-needle
like
OB-fold
gp27-like
200Å
115Å
85Å
H
30 Å
45 Å

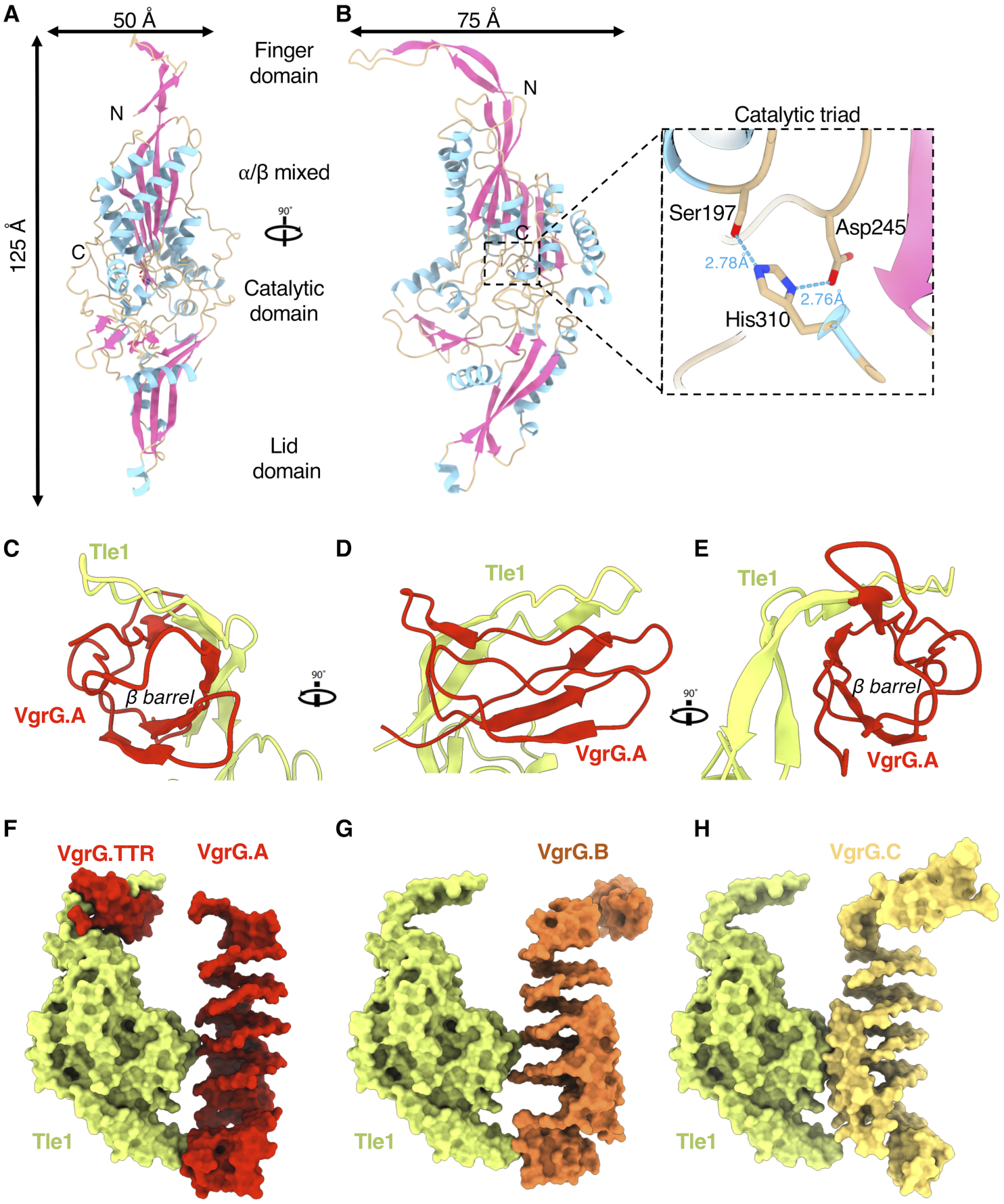
A
50 Å
125 Å
Finger domain
N
α/β mixed
90°
C
Catalytic domain
Lid domain
B
75 Å
N
C
Catalytic triad
Ser197
Asp245
2.78Å
2.76Å
His310
C
Tle1
VgrG.A
β barrel
90°
D
Tle1
VgrG.A
E
Tle1
β barrel
90°
VgrG.A
F
VgrG.TTR
VgrG.A
Tle1
G
VgrG.B
Tle1
H
VgrG.C
Tle1

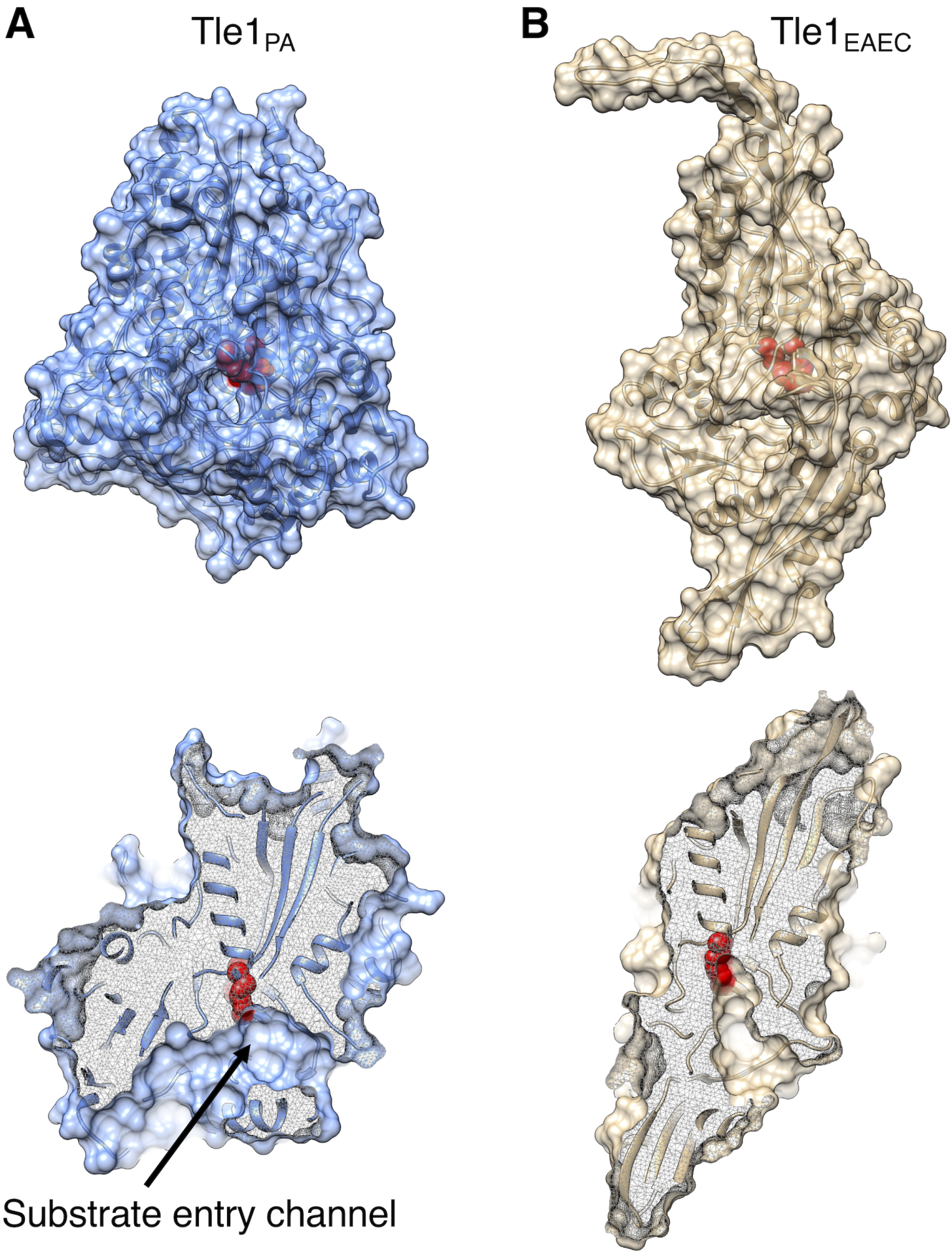
A
Tle1PA
B
Tle1EAEC
Substrate entry channel

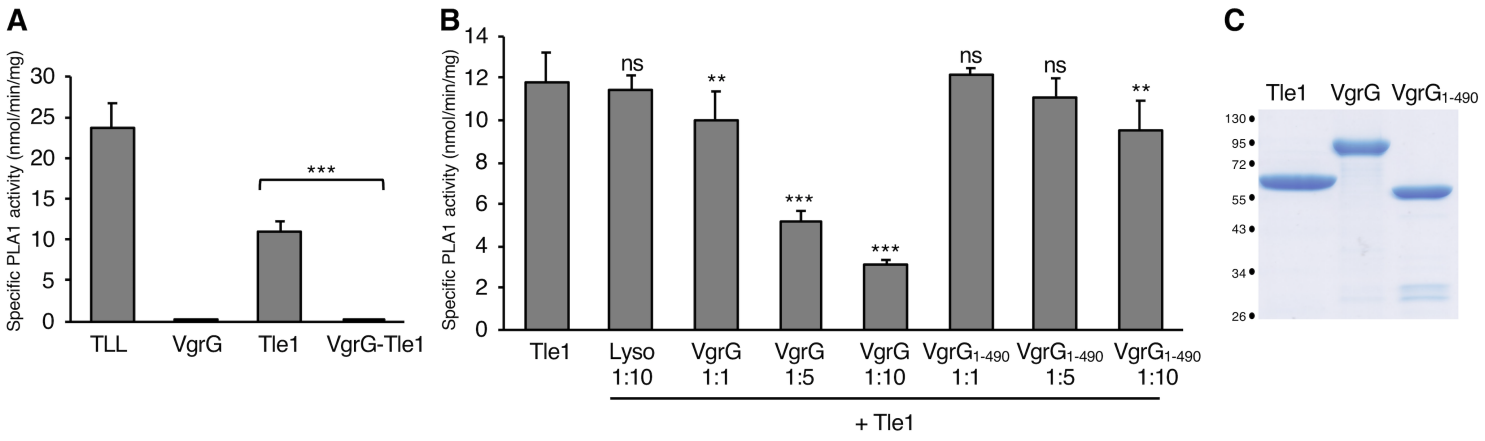
A
Specific PLA1 activity (nmol/min/mg)
30
25
20
15
10
5
0
***
TLL
VgrG
Tle1
VgrG-Tle1
B
Specific PLA1 activity (nmol/min/mg)
14
12
10
8
6
4
2
0
ns
**
***
***
ns
ns
**
Tle1
Lyso 1:10
VgrG 1:1
VgrG 1:5
VgrG 1:10
VgrG1-490 1:1
VgrG1-490 1:5
VgrG1-490 1:10
+ Tle1
C
Tle1
VgrG
VgrG1-490
130
95
72
55
43
34
26

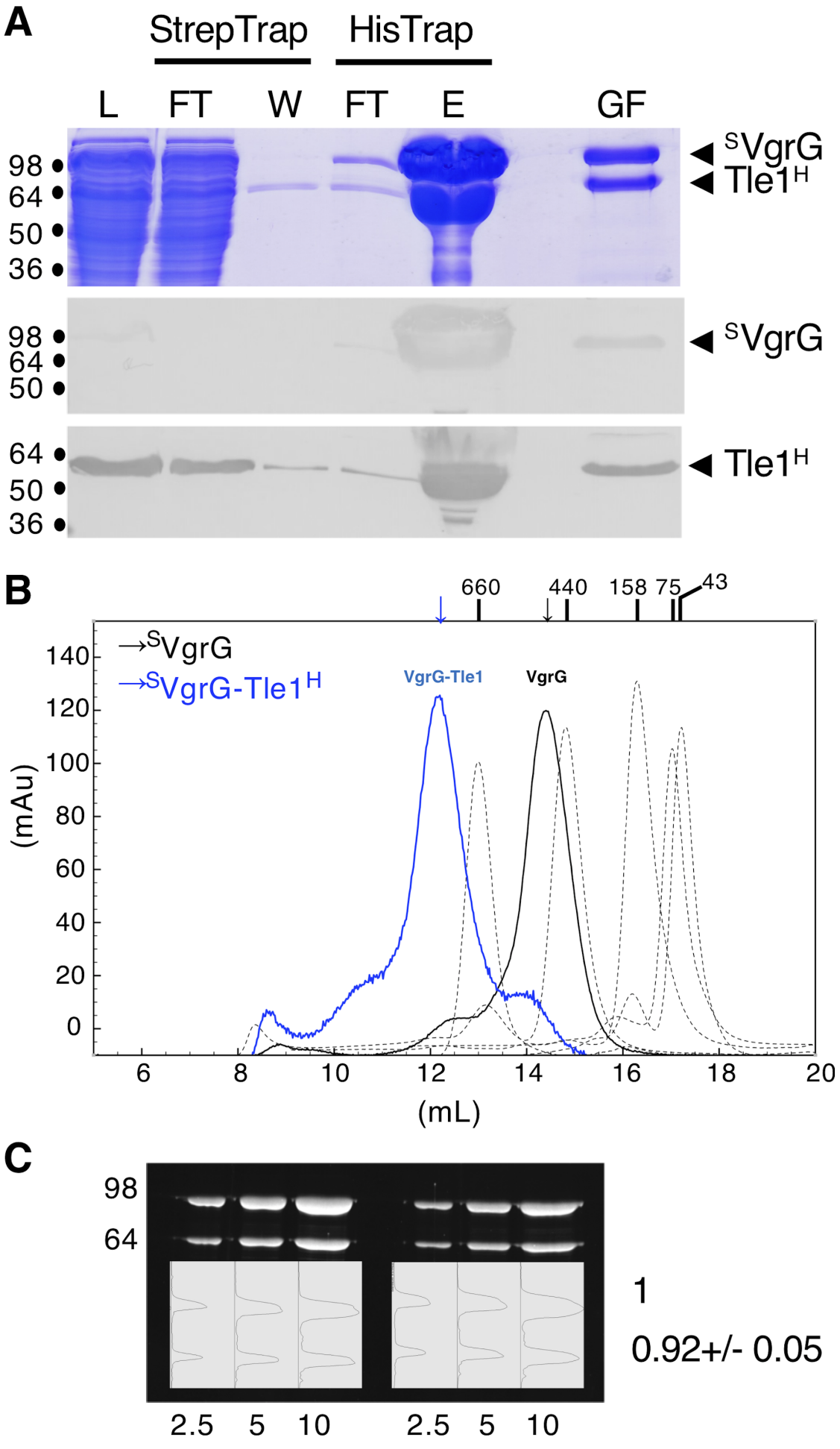
A
StrepTrap
HisTrap
L
FT
W
FT
E
GF
98
64
50
36
SVgrG
Tle1H
B
660
440
158
75
43
→SVgrG
→SVgrG-Tle1H
VgrG-Tle1
VgrG
(mAu)
(mL)
C
98
64
2.5
5
10
2.5
5
10
1
0.92+/- 0.05

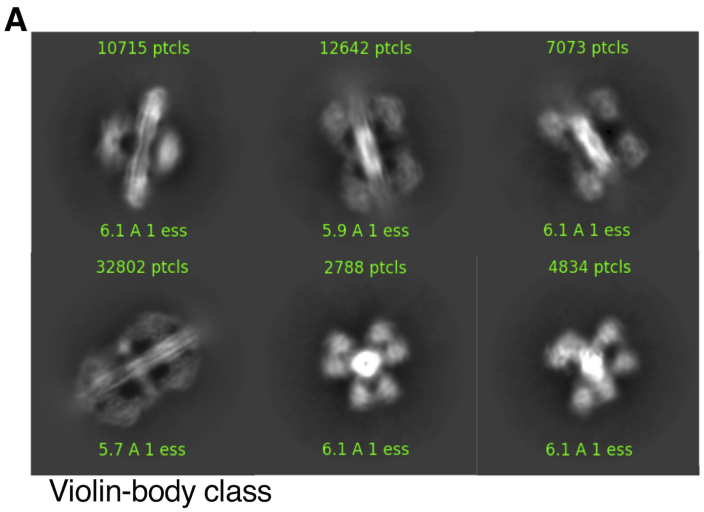
A
10715 ptcls
12642 ptcls
7073 ptcls
6.1 A 1 ess
5.9 A 1 ess
6.1 A 1 ess
32802 ptcls
2788 ptcls
4834 ptcls
5.7 A 1 ess
6.1 A 1 ess
6.1 A 1 ess
Violin-body class

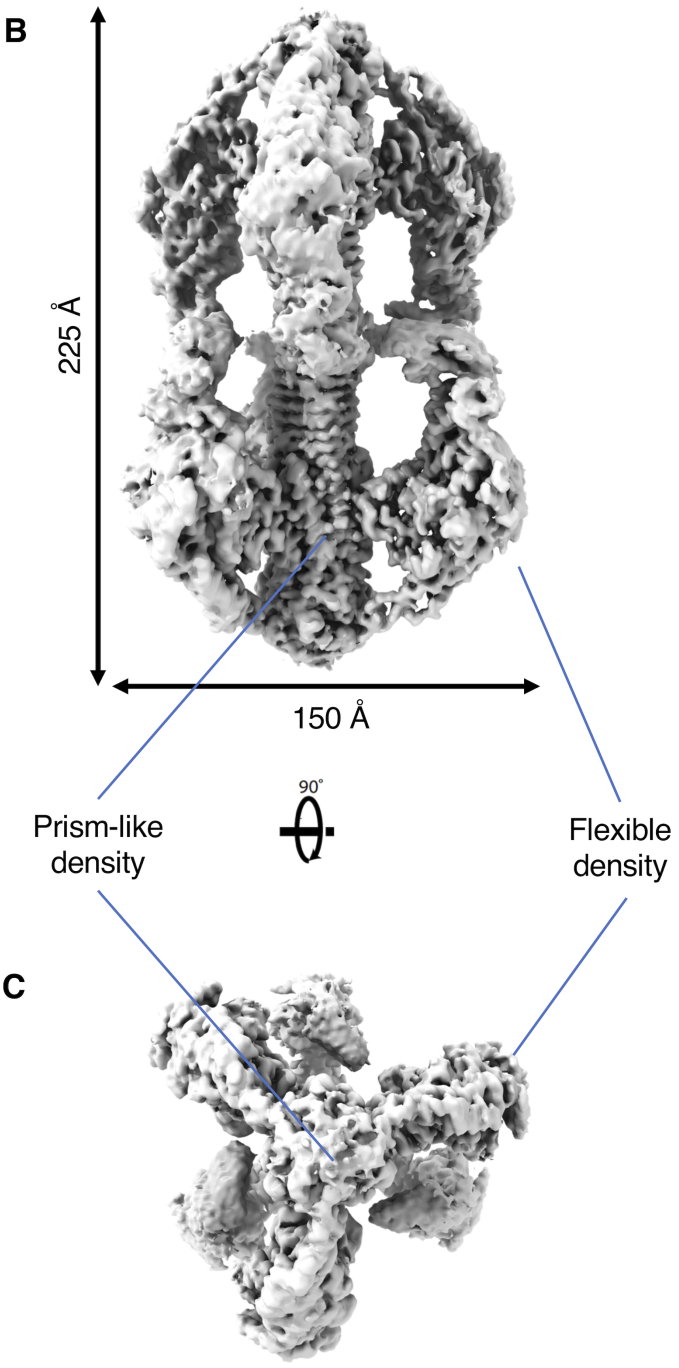
B
225 Å
150 Å
90°
Prism-like density
Flexible density
C

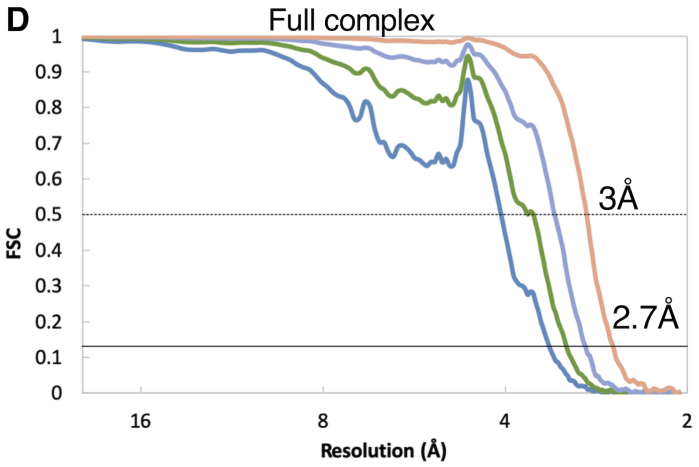
D
Full complex
FSC
Resolution (Å)
3Å
2.7Å

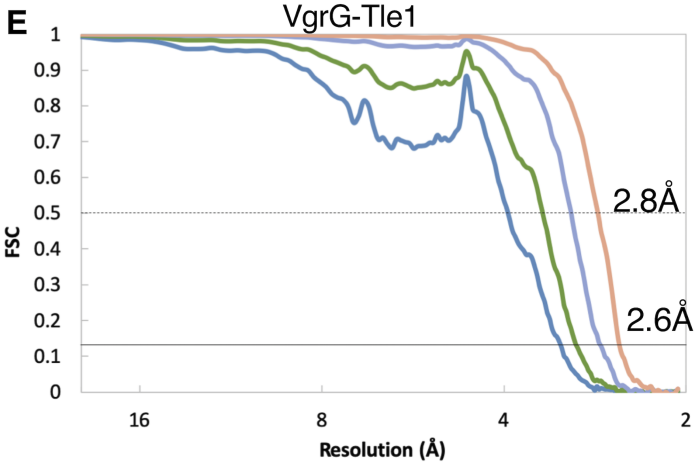
E
VgrG-Tle1
FSC
Resolution (Å)
2.8Å
2.6Å

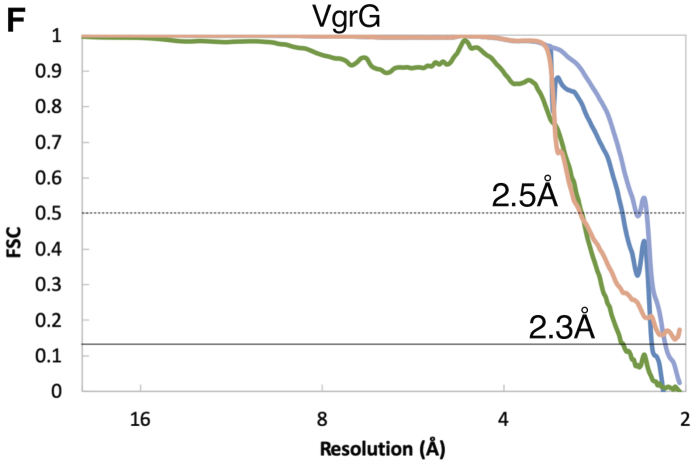
F
VgrG
FSC
Resolution (Å)
2.5Å
2.3Å

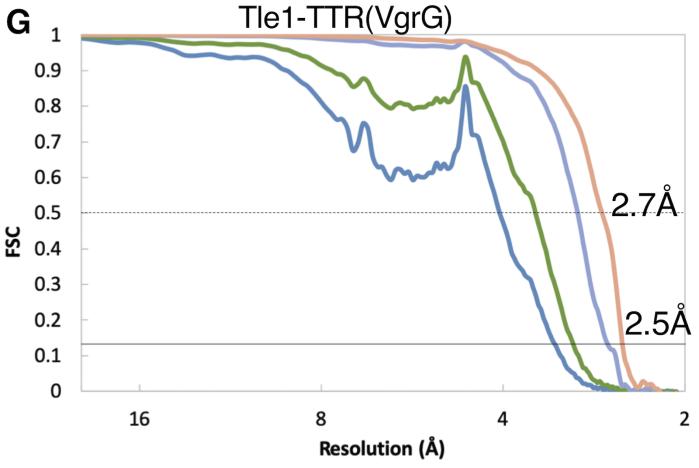
G
Tle1-TTR(VgrG)
FSC
Resolution (Å)
2.7Å
2.5Å

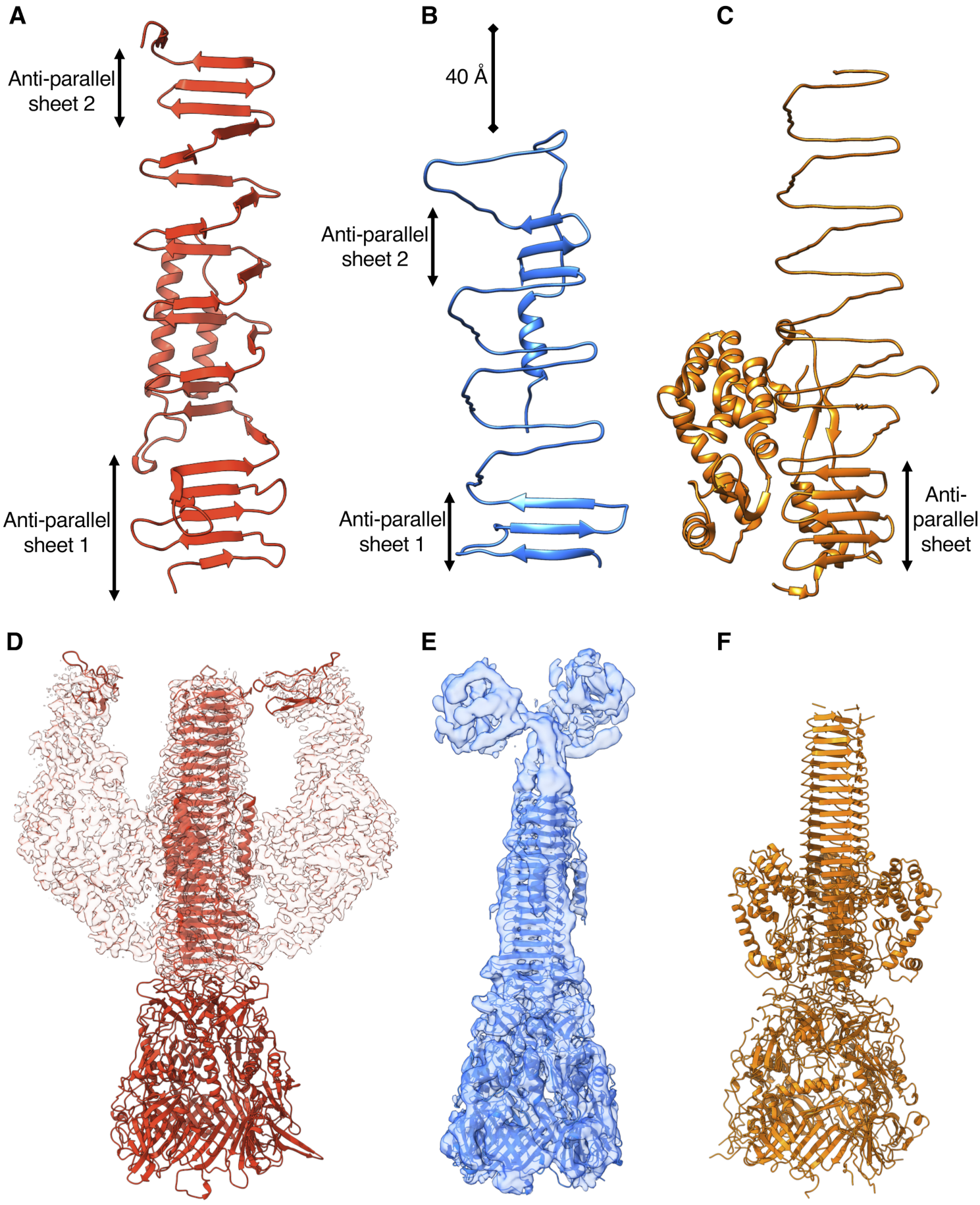
A
Anti-parallel sheet 2
Anti-parallel sheet 1
B
40 Å
Anti-parallel sheet 2
Anti-parallel sheet 1
C
Anti-parallel sheet
D
E
F

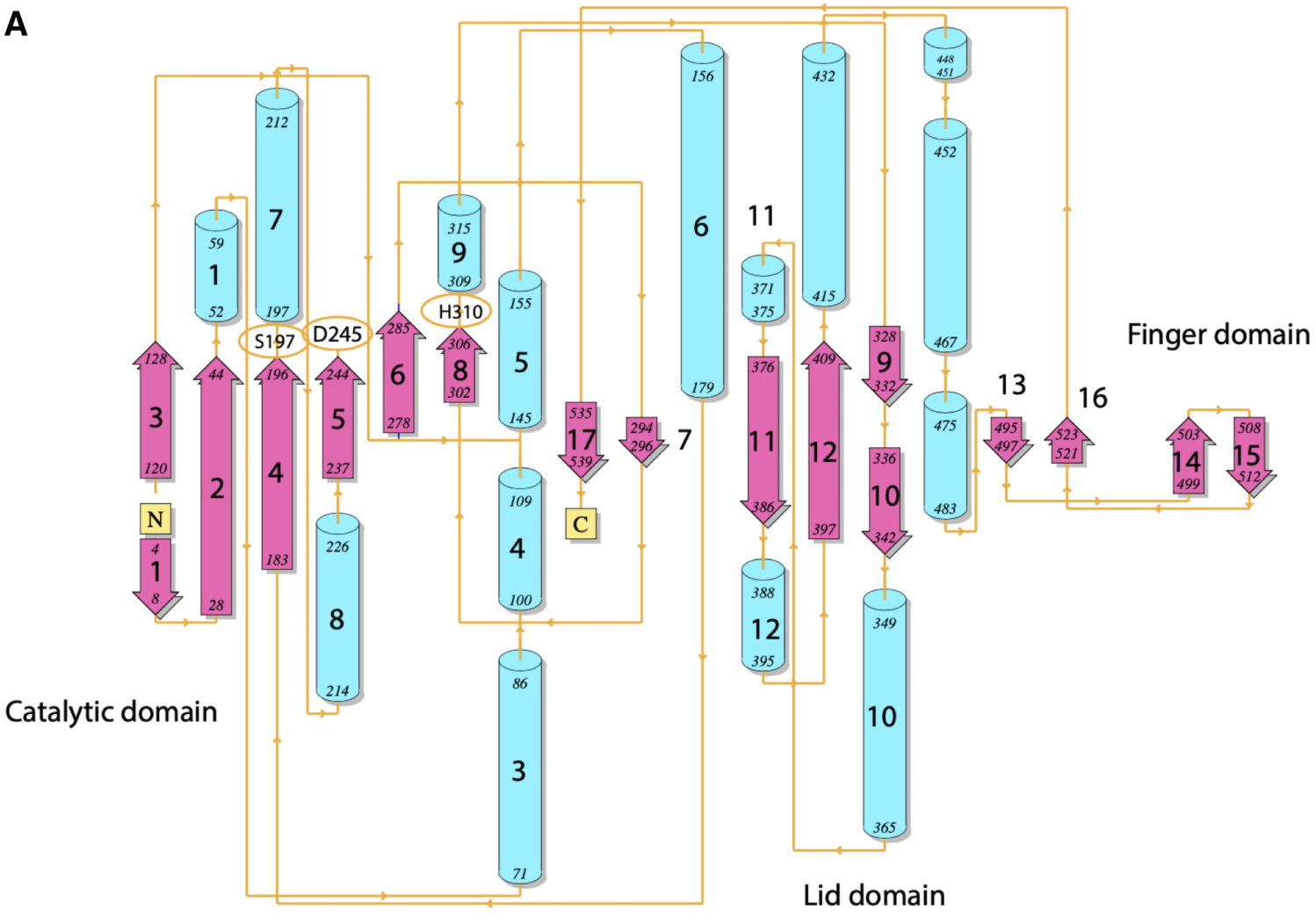
A
Catalytic domain
Lid domain
Finger domain
S197
D245
H310
N
C
B
90°
C

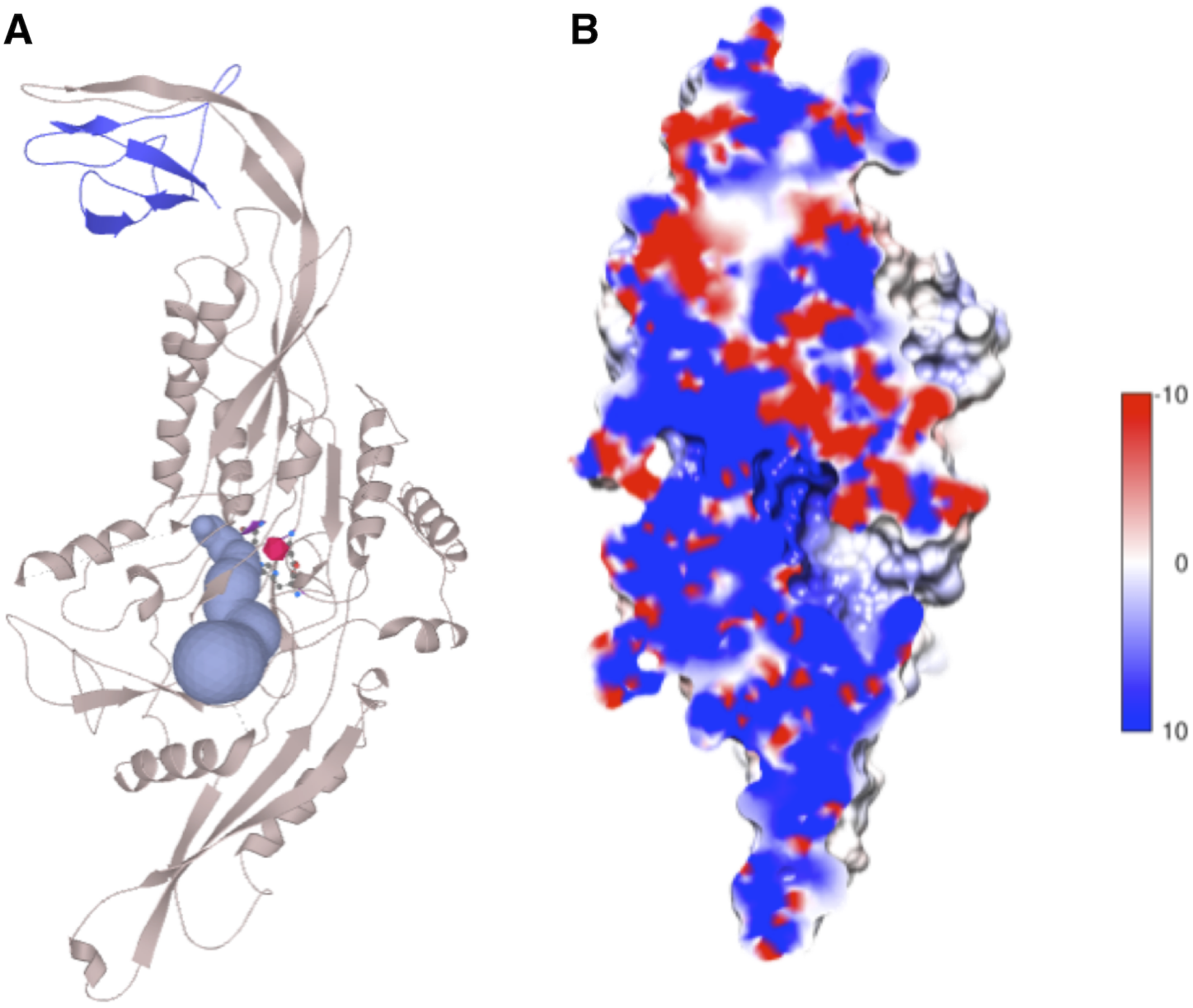
A
B
10
0
10